FABRICATION AND CHARACTERIZATION OF COBALT-DIAMOND-LIKE CARBON (Co-DLC) NANOCOMPOSITES

by

GUNJAN SHEBE

Presented to the Faculty of the Graduate School of

The University of Texas at Arlington in Partial Fulfillment

of the Requirements

for the Degree of

MASTER OF SCIENCE IN MATERIALS SCIENCE AND ENGINEERING

THE UNIVERSITY OF TEXAS AT ARLINGTON

December 2007

ACKNOWLEDGEMENTS

I would like to express my sincere gratitude to Dr. Efstathios I. Meletis for providing me the opportunity to work on this project. He has been a source of constant inspiration for me.

I would also like to thank Dr. Shaoxin You for helping me with all the information and support required for TEM. I am also thankful to Dr. Jin and Dr. Hao for accepting to be committee member.

I would like to express my gratitude to my parents and sisters for their unbounded care and love. It's because of their love, support and encouragement that I have reached this stage. I am grateful to both my friends Pallavi and Shan for their constant support throughout my research and stay at University.

I would also like to thank Dr. Ping Liu, Dr. Lee and Mr. Charles Savage for letting us use their facilities. I would like to express my gratitude to all my lab members especially Pankaj Hazarika and Jie He. I am also thankful to Mark, Narayan and Lei for their help.

December 13, 2007

ABSTRACT

FABRICATION AND CHARACTERIZATION OF

COBALT-DIAMOND-LIKE CARBON

(Co-DLC) NANOMPOSITES

GUNJAN SHEBE, MS

The University of Texas at Arlington, 2007

Supervising Professor: Efstathios I. Meletis

In recent years, synthesis of magnetic nanocomposites has been receiving significant attention. These nanocomposites offer opportunities to develop active nanomaterials with various applications like magnetic data storage and biomedical applications. They can be designed to provide excellent magnetic properties. However, high saturation magnetization materials, such as Co are not biocompatible. Thus, designing nanocomposites with magnetic phase embedded in biocompatible protective shells is of immense interest.

In this study, Co-DLC nanocomposites were synthesized using a hybrid CVD/PVD technique and different combination of processing parameters were used to vary the concentration of Co in the nanocomposites. X-ray photoelectron spectroscopy

showed, that with increase in the Co content from 50 at% to 65 at% the sp^3/sp^2 ratio decreases from 1.3 to 0.87 that consequently decrease hardness from 11.3 GPa to 9 GPa. An increase in the Co content was observed to increase the coefficient of friction. TEM images for all the nanocomposites from 25 at% to 65 at% showed Co nanocolumns encapsulated by DLC matrix. The nanocolumn exhibited wide variation from 6 nm to 14 nm. As-deposited Co-DLC was found to have ε-Co and DLC matrix. Magnetic measurements for as-deposited films illustrated that, nanocomposites with lower Co content and having small particles size shows superparamagnetic behavior, whereas nanocomposite with higher Co content of 65 at% showed ferromagnetic behavior. On annealing at 250^{o}C and 500^{o}C, all the nanocomposites exhibited ferromagnetic behavior accompanied by increase in the coercivity and saturation magnetization. On annealing at 500^{o}C, nanocomposite with 65 at% Co showed dramatic increase in the saturation magnetization and coercivity. Thus, annealing treatment can be used to tailor the magnetic properties of the nanocomposites and makes it suitable for various applications like sensor and biological.

TABLE OF CONTENTS

ACKNOWLEDGEMENTS…… ii

ABSTRACT…….. iii

LIST OF ILLUSTRATIONS……. viii

LIST OF TABLES……. x

Chapter

1. INTRODUCTION…… 1

2. OBJECTIVES…….. 4

3. LITERATURE REVIEW…….. 5

3.1 Magnetic Nanocomposites…… 5

3.1.1 Background…… 5

3.1.2 Shelled Magnetic Nanoparticles……. 10

3.1.3 Applications…….. 10

3.2 Diamond-like Carbon Thin Films…… 13

3.2.1 Deposition Techniques…….. 14

3.2.2 Classification and Characterization…… 18

3.2.3 Mechanical Properties…… 21

3.3 Cobalt-Carbon (Co-C) Nanocomposites…….…….. 25

3.3.1 Deposition Techniques……...……. 26

3.3.2 Co-C Nanocomposite Structure…..……... 26

3.3.3 Magnetic Properties…….……...….. 28

3.3.4 Co-a-C:H Nanocomposites……... 30

4. EXPERIMENATL PROCEDURE…… 33

4.1 Experimental Set Up…….. 33

4.2 Deposition of Co-DLC Nanocomposites……. 34

4.3 Characterization of Co-DLC Nanocomposites……..…… 35

4.3.1 Composition…….. 35

4.3.2 Thickness and Roughness…….. 35

4.3.3 Transmission Electron Microscopy (TEM)…… 35

4.3.4 X-Ray Photoelectron Spectroscopy (XPS)…… 37

4.3.5 Fourier Transform Infrared Spectrometry (FTIR)…..…….. 39

4.4 Mechanical Testing…..…… 39

4.5 Tribological Testing……...……. 40

4.6 Magnetic Properties…… 40

4.7 Annealing Experiments…… 40

4.8 Shelled Co/DLC Nanoparticles……...……... 41

5. RESULTS AND DISCUSSION..... 44

5.1 Deposition of Nanocomposites and Effect of Processing Parameters …… 44

5.2 Thickness and Roughness…… 46

5.3 TEM Analysis..... 49

5.4 XPS Analysis……...……..…….. 53

5.5 FTIR Analysis…….…… 56

5.6 Mechanical Properties…… 60

5.7 Tribological Properties…… 62

5.8 Magnetic Properties…….…… 63

5.9 Annealing Experiments …….…… 66

5.10 Shelled Co/DLC Nanoparticles……..……..... 75

6. CONCLUSIONS……..……...…….. 78

REFERENCES……... 80

BIOGRAPHICAL INFORMATION……. 86

LIST OF ILLUSTRATIONS

Figure Page

3.1 Magnetic moment for (a) Paramagnetic Material (b) Ferromagnetic Material (c) Antiferromagnetic Material (d) Ferrimagnetic Material……. .. 7

3.2 Magnetic Flux Density versus Magnetic Field Strength curve for Ferromagnetic Material (Hystersis Curve)…… 9

3.3 The sp^3, sp^2 and sp^1 hybridized bonding ……..... 14

3.4 Ternary phase diagram for hydrogen free and hydrogenated amorphous carbon……..... 19

3.5 Loading-unloading curve for nano-indentation measurement of ta-C:H…… 22

3.6 Variation of nano-hardness of ta-C with sp^3 fraction…….. 23

4.1 Schematic of the deposition system…..…….. 33

5.1 The effect of pressure on Co content in the Co-DLC nanocomposite films……..... 45

5.2 (a) Thickness three dimensional display and (b) Thickness profile for Nanocomposite 4.....……..... 47

5.3 (a) Roughness three dimensional display and (b) Roughness profile for Nanocomposite 4.....……..... 48

5.4 Cross sectional TEM images for Co-DLC Nanocomposites (a) 4 and (b) 7…… 50

5.5 Plan view TEM image for Co-DLC Nanocomposite 5……... 51

5.6 Plan view TEM image for Co-DLC Nanocomposite 4……... 52

5.7 Plan view TEM image for Co-DLC Nanocomposite 7……... 52

5.8 DP for Co-DLC nanocomposite 4.....……..... 52

5.9 High resolution spectra for C 1s electron for
(a) Nanocomposite 4 and (b) Nanocomposite 7…….... 54

5.10 Deconvoluted FTIR spectra for C-H stretch bonds for
(a) Nanocomposite 7 and (b) Nanocomposite 4……. 58

5.11 Variation of microhardness with the percentage cobalt
present in the Co-DLC nanocomposites …….... 61

5.12 Variation of the Coefficient of friction as a function of sliding
distance for DLC and Co-DLC Nanocomposites 4 and 7……. 62

5.13 Magnetization-Magnetic field (M-H) hystersis curve for
Co-DLC Nanocomposite 4, 5 and 7 for (a) in plane
and (b) out of plane applied magnetic field……..……. 64

5.14 High-resolution spectra of C 1s electron for
Co-DLC Nanocomposite 4 (a) as-deposited and
(b) annealed at 250^{o}C……..…….……..... 67

5.15 In plane Magnetization-Magnetic field hystersis curve for
(a) Nanocomposite 5, (b) Nanocomposite 4 and (c) Nanocomposite 7,
annealed at 250^{o}C and 500^{o}C…..…… 70

5.16 Out of plane Magnetization-Magnetic field hystersis curve for
(a) Nanocomposite 5, (b) Nanocomposite 4 and (c) Nanocomposite 7
annealed at 250^{o}C and 500^{o}C…..…… 73

5.17 TEM image of Co-DLC thin film deposited on the copper grid…….. 75

5.18 Si substrate with polystyrene particles……. 76

5.19 Si substrate and polystyrene particles with Co-DLC thin film……. 76

5.20 Si substrate after dissolving polystyrene particles…… 77

LIST OF TABLES

Table Page

3.1 Comparison of properties of different states of carbon …….. 20

3.2 Comparison of various techniques used to determine sp^3 and hydrogen content 21

3.3 Elastic properties for various states of Carbon …… 23

4.1 Binding energies for C1s electrons ….……...……... 38

5.1 Processing parameters and composition for the selected nanocomposites…… 44

5.2 Thickness, roughness and deposition rate for Co-DLC nanocomposites...…..... 46

5.3 Percentage of four C states and overall composition of the nanocomposites.……...…….… 55

5.4 Assignment of C-H stretch bonds for Co-DLC Nanocomposites 4 and 7……..……. 59

5.5 The percentage of different states of C 1s electron spectrum and overall composition of Nanocomposite 4……..… 68

5.6 Magnetic properties for Co-DLC nanocomposite 5, 4 and 7.……... 71

5.7 Magnetic properties for Co-DLC nanocomposite 5, 4 and 7……..... 72

CHAPTER 1

INTRODUCTION

The multi disciplinary applications of nanocomposites are growing day by day as these materials exhibit unique combination of mechanical, tribological, magnetic and electronic properties. It has been reported that nanocomposites with size less than 100 nm display novel properties as compared to their microscale counterparts. These nanocomposites can be tailored to enhance their properties thus, increasing their potential applications in various fields.

In the last few years, Co-C nanocomposites have attracted tremendous attention due to their electronic, MEMS, magnetic and photonic applications. Co-C thin films have been synthesized and studied for their structural, tribological, mechanical and magnetic properties. Co-C thin films were investigated to study the microstructural evolution of Co nanostructure with respect to annealing temperature. It was reported that, as-deposited Co-C thin films show highly defected ε-Co structure. On annealing at higher temperature at around 360^{o}C, ε-Co transforms to α-Co or β-Co[1]. Thus, the post deposition annealing treatment can be used to control the structure and magnetic properties of the Co-C nanocomposites. Replacing carbon with diamondlike carbon (DLC) can further enhance the properties of nanocomposites making them multifunctional. DLC are amorphous hydrogenated carbon films composed of a combination of sp^3 and sp^2 bonded carbon. These films possess a unique combination of

mechanical, tribological, physical, biological and chemical properties. DLC coatings are inert and they increase the stability of surface and protect the substrate from corrosion and oxidation[2]. DLC films provide low friction and high wear resistance to sliding contact interface thus, enhancing the tribological properties[3, 4]. DLC is biocompatible, extremely hard, and chemically inert and does not suffer from thermally induced stresses which make it a beneficial biomaterial[5-7]. However, DLC films have some limitations such as high internal stresses, low toughness and adhesion which can be overcome by doping with a metal element and forming Me-DLC.

In the last few years, studies on various Me-DLC films such as, Si-DLC, Ti-DLC, C-Ag-Pt-DLC, Cr-DLC and others have been reported[8-11]. Me-containing DLC films provide a new phase along with controllable variation of properties. In multifunctional Co-DLC nanocomposites, both Co and C act in a synergic fashion giving superior mechanical, tribological and magnetic properties.

Up to date limited research is available on Co-DLC nanocomposites. Local structure of Co nanocrystal embedded in hydrogenated amorphous carbon was studied by Kolobov[12]. Synthesis of Co cluster in polymerized hydrocarbon and their magnetic behavior was reported by Laurent et al[13-14]. Wang et al synthesized Co-DLC thin films using a hybrid PECVD/PVD technique and systematically investigated the microstructural evolution, structure-property relationship of the thin films[15-17]. Both Laurent et al and Wang et al reported that, Co in Co-DLC thin films changes phase from ε-Co to HCP-Co on annealing. These results are in agreement with the microstructural evolution of previously reported Co-C thin films[1]. At present, there is

no detailed analysis of the effect of annealing on magnetic properties of Co-DLC nanocomposites. This study aims at synthesis and characterization of Co-DLC nanocomposites using a newly build PECVD/PVD system, with reference to the earlier work reported by Wang et al. Investigate the effect of annealing and size of Co nanoparticles on the magnetic properties of these nanocomposites and thus, eventually produce Co nanoparticles encapsulated by DLC matrix to suit various applications.

CHAPTER 2

OBJECTIVES

In multifunctional Co-DLC nanocomposites both cobalt and carbon act in a synergetic fashion in terms of properties and thus, have the potential to increase their field of applications. Recently, Wang et al deposited Co-DLC thin films using a PECVD/PVD method, and studied the structure-property relationship and the microstructural evolution of Co-DLC nanocomposites with respect to the annealing temperature[15-17]. As reported earlier, Co in Co-DLC changes from ε-Co to HCP-Co on annealing. So the properties of the nanocomposites can be tailored to suit various applications.

The objective of the present study is to synthesize Co-DLC nanocomposites using newly build PECVD/PVD system at Surface and Nano-engineering Laboratory, with reference to the earlier work reported by Wang et al. Characterize Co-DLC nanocomposites using various techniques like TEM, XPS, FTIR. Study the mechanical, tribological and magnetic properties of the nanocomposites. Study the effect of annealing on the microstructure and magnetic properties, so to explore their potential applications. Finally, making Co/DLC nanoparticles that can be used for various applications like sensors and biological.

CHAPTER 3

LITERATURE REVIEW

3.1 Magnetic Nanocomposites

The history of magnetism dates back to thousands of years, but the understanding of basic principles and the phenomenon related to magnetism developed only in the twentieth century. Lodestone, a mineral form of iron, is supposed to be the first material showing magnetism. From the twentieth century, progress of magnetic materials took place from macroscopic scale to nano particles. Electromagnet and compass needle are examples of macroscopic magnetic materials. Recently, the focus of research shifted from micro scale to nano scale magnetic materials, driven by technological demands.

Materials with size less than 100 nm are called nanomaterials. Depending on their geometry, magnetic nanostructures can be classified into five different groups as particles and clusters, thin films and mulitlayers, particle arrays and functional components, nanowires, nanocomposites and other bulk materials[18]. These nanostructures provide wide array of properties and thus have widespread applications.

3.1.1. Background

The magnetic field and dipole explain the basic concept of magnetism. Volume of space where the magnetic forces act is termed as magnetic field. The magnetic field

can be detected with the aid of magnetic dipoles. Magnetic dipoles are the bar magnets with the North and South Pole at each end of the magnet.

The magnetic properties of the material are contributed by magnetic moment of each electron. As per quantum mechanics, the magnetic moment for electrons originates from two sources. One is the orbital motion of the electron around the nucleus generating magnetic moment along the axis of rotation. Other magnetic moment is generated by the electron spin along the direction of the spin axis. Magnetic materials can be classified into five different categories as diamagnetic, paramagnetic, ferromagnetic, ferrimagnetic and antiferromagnetic based on their response to the applied magnetic field.

Magnetic permeability (μ) is the ratio of flux density (B) to the magnetic field strength (H). Magnetic flux density is the magnetic flux per unit area perpendicular to the direction of flux; its units are Tesla (wb/m^2). Magnetic field strength is the amount of magnetic flux perpendicular to the direction of the flux; its units are Henry (amp/m). So $\mu = B / H$ and the units of permeability are henry per meter. Relative permeability (μ_r) is the ratio of magnetic permeability (μ) to the permeability of vacuum (μ_0). So $\mu_r = \mu / \mu_0$ and it is a dimensionless quantity. Magnetic susceptibility is defined as $\chi = M / H$, where M is magnetization i.e. magnetic moment per unit volume and the H is applied magnetic field. Magnetic susceptibility is a dimensionless quantity[19-20].

Diamagnetic materials are not permanently magnetic due to cancellation of all the electron spin and it shows magnetism only in the presence of externally applied magnetic field. The moment is induced due to change in the orbital motion of the

electron due to applied magnetic field. For diamagnetic materials relative permeability, μ_r is less than one and magnetic susceptibility is negative.

Material with positive magnetic susceptibility and relative permeability, μ_r greater than unity is called a paramagnetic material. This material shows permanent dipole moment due to incomplete cancellation of electron spin but they are randomly orientated. On applying external magnetic field the magnetic pole align parallel to the applied field. Elements like Pt, Mn are paramagnetic.

Some transition metals like Fe, Ni, Co show very large permanent magnetism even in the absence of externally applied magnetic field, these materials are termed as ferromagnetic materials. They have magnetic susceptibility as high as 10^6 and higher permeability. Permanent magnetic moment is the result of the atomic magnetic moment due to electron spin and uncancelled electron spin. The coupling interaction causes net spin magnetic moment to align parallel to each other even in absence of externally applied magnetic field. Ferromagnetic materials show spontaneous magnetization called as saturation magnetization. Ferromagnetic materials are used widely in industry.

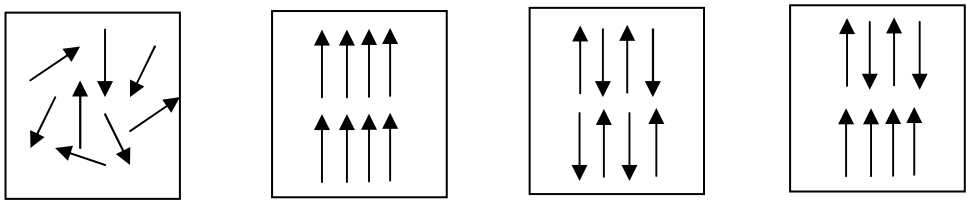

Figure 3.1 Magnetic moment for (a) Paramagnetic Material (b) Ferromagnetic Material (c) Antiferromagnetic Material (d) Ferrimagnetic Material.

The material with both parallel as well as antiparallel magnetic moment is termed as antiferromagnetic material. They have positive but small susceptibility.

Manganese oxide (MnO) shows antiferromagentic behavior. Some ceramic materials show permanent magnetism called as Ferrimagnetism. These atoms have anti parallel magnetic moments. They have large and positive permeability. Figure 3.1 shows the magnetic moment for different types of magnetic materials.

All ferromagnetic and ferrimagnetic materials are made up of small volume region, called as domain. In each domain, local magnetization is saturated. A Bloch Wall is the transition layer in the crystal that separates adjacent domains. Thus, a material is made up of many domains and each of the domains may have different magnetization. When a magnetic field is applied the domain changes shape and size by the movement of domain walls. This explains the hystersis curve for magnetic materials.

Hysteresis curve is the plot of magnetic flux density (B) versus the applied magnetic field (H). The magnetic material can also be classified as a hard magnetic material, soft magnetic material and magnetic storage. The hard magnetic materials show high remanence (B_r), coercivity (H_c) and saturation flux density (B_s). They also show low initial permeability and high hystersis energy losses. Coercivity is the negative H field applied in direction opposite to the applied field H, in order to reduce the B field to zero. Remanence (B_r) is the residual B field that exists at zero H field on demagnetization after saturation. A hard magnet also shows higher Curie temperature (T_c). Curie temperature is the temperature at which ferromagnetic material loses its ferromagnetism and becomes paramagnetic. Soft magnetic materials have high initial permeability and low coercivity (H_c). They have low hysteresis loss per cycle and high

Curie temperature (T_c)[21-22]. Figure 3.2 shows the hystersis curve for a magnetic material[21].

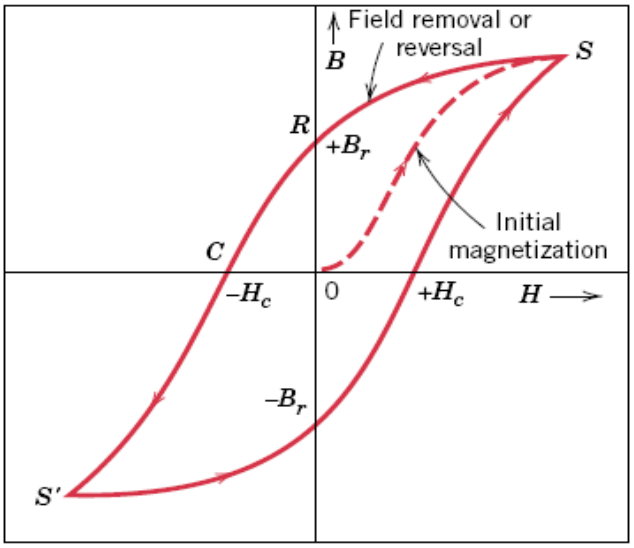

Figure 3.2 Magnetic Flux Density versus Magnetic Field Strength curve for Ferromagnetic Material (Hystersis Curve)[21].

The shape of hystersis curve depends on various factors such as crystallinity, i.e. specimen is single crystal or polycrystalline, preferred orientation of grains in polycrystalline sample, presence of second phase particles and temperature or stress level. This dependence of magnetic behavior on crystallographic behavior is termed as magnetic anisotropy.

Cobalt is a hard ferromagnetic material and widely used in magnetic steels and stainless steels. Cobalt in form of alloys is used for high-speed, heavy-duty, high temperature cutting tools, and for dies.

3.1.2. Shelled Magnetic Nanoparticles

Recently magnetic nanoparticles have been the focus of increasing research due to their extensive applications in various fields. Magnetic nanoparticles can be synthesized by different top down and bottom up techniques.

In last few years, fabrication of shelled magnetic nanoparticles is an area of great interest. Chemical synthesis is one of the widely used methods for fabrication of magnetic nanoparticles. In these methods, magnetic materials, like iron and cobalt, are used. Iron and cobalt are prone to oxidation. So, magnetic nanoparticles are typically encapsulated by a non magnetic inert matrix forming shelled nanoparticles. This non magnetic matrix needs to be biocompatible while it protects the magnetic nanoparticles from oxidation. The matrix also prevents interaction between the magnetic nanoparticles. Nanoparticles encapsulated by biocompatible material have wide application as Magnetic Resonance Imaging (MRI) contrast agent, hyperthermia treatment and targeted drug delivery.

3.1.3 Applications

Cobalt and iron can exist in multiple crystal phases resulting in crystalline anisotropy[23]. The magnetic properties of these nanocomposites can be tailored to suit different applications. Some of the applications of magnetic thin films and magnetic nanoparticles are briefly discussed in this section.

a. Magnetic thin films in Magnetic Data Storage

Magnetic thin films are used in devices such as magneto optical recording, magnetic and microwave circuits, magnetic recording media etc. Earlier tape media

were made up of Fe_2O_3 particles that later were replaced by magnetic thin films. Density of the high recording media changed tremendously after the use of thin films. Introduction of Giant Magnetoresistance led to the further increase in the storage density of the recording media reaching around 200 Gbits/inch^2 for longitudinal recording[24].

Co based and Fe based thin films are used for recording[25]. Storage density is increased by decreasing the area used to store one bit of data. Magnetic properties of the nanocomposites can be optimized by changing the size of the nanocomposites[26]. The nanocomposites of Co carbon thin films deposited on recording heads improve tribological properties at the head disk interface, prevent mechanical wear and protect transducer against corrosion[27]. The thin films should be atomically smooth, dense, continuous and pin hole free[24].

b. Magnetic Resonance Imaging

MRI is primarily used in medical imaging to demonstrate the alteration of the living tissues in the body. MRI measures changes in magnetization of hydrogen proton in water molecules sitting in a magentic field after a pulse of radio frequency has hit them. Protons from differnet tissues react differnetly giving a picture of anatomical structures[28]. Contarst agents sharpen the contarst by affacting the behavior of protons in their proximity, thus, enhancing the imaging. MRI contarst agents in standard MRI scans travel through the bloodstream and tissues, thus, increaing the contarst of the tissues that come in contact with it[28].

Transition metals with paramagentic properties are generally used for MRI imaging as these particles provide contarst enhancement by alterating the local magnetic enviornment. Iron oxide nanoparticles are commonly used contarst agents as dipolar interaction between the superparamagentic core and the surrounding solvent protons increases the relaxation time[29]. Shelled magnetic nanoparticles are prefered for imaging as the shelled structure prevents oxidation of the nanoparticles[30].

c. Hyperthermia Treatment

Hyperthermia treatment involves destroying the body tissue by aid of heat generated by magnetic materials. Magnetic material in self controlled hyperthermia treatment is introduced near the tumor. The magnetic material subjected to the oscillating magnetic filed generates heat by hystersis loss and destroys the tumor cells. Magnetic materials with low Curie temperature are suitable for this treatment. Once a material reaches the Curie temperature, it stops responding to applied alternating field and thus, controls overheating of the tumor cells and also prevents healthy tissues.

Superparamagnetic iron oxide nanoparticles have extraordinary absorption rate which makes them suitable for hyperthermia treatment[31]. Non-toxicity, biocompatibility, injectibility and high level accumulation in the target tumor are the important properties of the magnetic nanoparticles for inducing hyperthermia treatment[32].

d. Drug Deliver

Pharmaceutical drugs attached to the surface of the magnetic nanoparticles are directed to the target organ and are released[33]. Localized magnetic field gradient attracts

the particles to the targeted site and retains them at that site till the completion of process and removal of particles. When the forces generated by externally applied magnetic field exceed the linear blood flow rate the nanoparticles are retained at the targeted site[34]. The size of the particle used for this application should be less than 100 nm.

Ferrite nanoparticles show biocompatibility, chemical stability, and adequate magnetic saturation. Superparamagnetic ferrite nanoparticles do not retain magnetization before and after exposure to the magnetic field and reduce agglomeration of the particles hence these particles are mostly used for targeted drug delivery[33, 35].

3.2 Diamond – like Carbon Thin Films

Diamond like Carbon (DLC) is an amorphous (a:C) or hydrogenated amorphous (a-C:H) form of carbon consisting of diamond-like and graphite-like domains. DLC has a significant fraction of sp^3 bonding which confers on it many of the beneficial properties of diamond, whereas sp^2 bonding of DLC confers on it properties of graphite[36, 37]. DLC films have been the subject of research from the past two decades due to their unique combination of properties including high hardness, low friction coefficient and wear rate, high electrical resistivity, high thermal conductivity, optical transparency, chemical inertness and biocompatibility[38, 39]. DLC coatings have wide applications as protective coatings for optical windows, magnetic storage disks, car parts, micro-electromechanical devices and biomedical coatings. There is an increasing interest in electronic applications as thin film cathode material for field emission displays[40] and biomedical applications for implantation[41].

Carbon exists in different allotropic forms such as diamond, graphite and polymer. Carbon can form a great variety of crystalline and disordered structures because it is able to exist in three hybridizations, sp^3, sp^2 and sp^1, as shown in Figure 3.3[36]. In sp^3 hybridization (tetrahedral) as in diamond, four valence electrons of carbon form strong σ bonds with four adjacent atoms. In sp^2 hybridization (trigonal) as in graphite, three of the four valence electrons form strong σ bonds and one weak π bond. In sp^1 hybridization (linear) there are two σ bonds and two π bonds. The outstanding properties of DLC confer to the presence of sp^3 bonding.

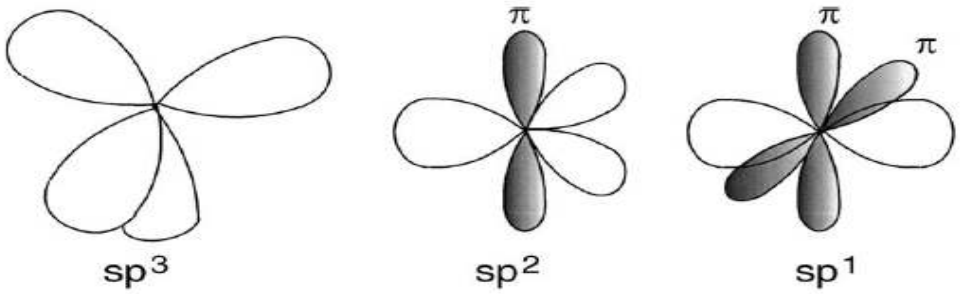

Figure 3.3 The sp^3, sp^2 and sp^1 hybridized bonding[36].

3.2.1 Deposition Techniques

Various kinds of Chemical Vapor Deposition (CVD) and Plasma-assisted deposition methods are used to synthesize DLC thin films. The CVD process involves decomposition of a carbon bearing gas phase on the substrate, while solid or vapor phase carbon is used in the plasma deposition. The most common methods include:

a. Direct Ion Beam Deposition

In the Ion Beam Deposition method, carbon ions are produced by ionization of hydrocarbon gases such as methane, ethane, etc. In ionization, the molecules

disassociate and most of the hydrogen is liberated[36, 41]. The substrate is bombarded by a beam of carbon and hydrocarbon ions having energy around 100-1000 eV[42]. It is the impact of these ions on the substrate leading to the formation of sp^3 bonds. Hydrogen is always incorporated in the film by this method. The process is carried out in high vacuum deposition chamber.

b. Mass Selected Ion Beam (MSIB)

MSIB gives controlled deposition rate from monoenergetic ion species. Carbon ions with low energies around 1-10 eV are produced from the graphite target[36]. The ions are accelerated to pass through magnetic filter; filters out neutral ions. C^+ ions with an e/m ratio are selected and are further accelerated. Electrostatic lenses decelerate the ions to the desired ion energies. Ion beam is focused on the substrate in high vacuum condition. The possibility of damage during deposition is less in high vacuum pressure condition[43]. The advantage of the process is that it allows control of the deposition rate and fraction of sp^3 bonds.

c. Filtered Cathodic Arc Deposition

The Cathodic Arc Deposition method is used to produce hydrogen free DLC coatings. An arc is created in high vacuum by striking a carbon electrode to the graphite cathode typically at 50-75 A which produces a dense plasma[36, 41]. The plasma is filtered by passing it through the magnetic filter. The magnetic filter filters out neutral species and particulates generated in the process. The plasma is condensed on the substrate which is negatively biased in the range of -20 to -350 V[44]. The advantage of the process

is that it produces extremely dense ionized plasma and higher deposition rate so it produces dense films.

d. Magnetron Sputtering

Sputtering is a process in which particles with high energy strike the surface, ejecting atoms or molecules of target material. For successful sputter deposition, ions of sufficient energy must be created and directed towards the target to remove atoms from the target. Secondly, ejected atoms must move freely to the substrate with little impedance to their movement. To maintain high ion energies and to minimize gas atom collision after ejection from the target, low pressure is maintained while sputtering[45].

The plasma needed for the process is generated by either DC or RF power. During sputtering under the adequate voltage across the electrode and appropriate gas pressure, the gas will breakdown and will form plasma discharge. Near the cathode, a high electric filed dark space or sheath is developed. Ions are accelerated rapidly along the sheath and strike the cathode. On collision secondary electrons are emitted from the surface. These electrons when accelerated towards the sheath gain more energy. The secondary electrons collide with gas atoms to form more ions. In DC mode the target directly conducts the electricity. While in the case of rf mode, alternating current at higher frequency is applied. The advantage of rf system is that for small part of rf cycle the cathode and anode are electrically reversed, eliminating charge build up on an insulating surface and providing equal number of ions and electrons. The secondary electrons are the main source of energy for plasma discharge and secondary electron yield is very low so magnetron sputtering is used [45].

Magnetron uses static magnetic field located parallel to the cathode. Secondary electrons emitted from the cathode are constrained to move in a direction perpendicular to both applied electric field and magnetic field. The secondary electrons are trapped in the region close to the cathode. On collision with gas atoms, extremely dense plasma is formed. Thus, magnetron sputtering increases sputtering yield resulting in high deposition rates [45].

e. Pulsed Laser Deposition

A Pulsed excimer laser is used to vaporize the target material which is generally graphite or polycarbonate[36, 41]. Intense energy pulses of excimer laser vaporize the target producing intense plasma which is deposited on the substrate in a high vacuum chamber. The substrate is either negatively biased or unbiased with respect to the target. It is a versatile method and can be used to deposit different materials[46]. It can be used to deposit both hydrogenated (a-C:H) and amorphous carbon (a-C) DLC coatings.

f. Plasma Enhanced Chemical Vapor Deposition (PECVD)

PECVD is one of the most popular methods used for DLC deposition. Hydrocarbon gases such as methane and ethane are used as the source gas. The technique involves various chemical processes of neutral species and dehydrogenation as well as physical processes like subplantation. The plasma deposition takes place in three stages as plasma reaction, plasma surface interaction and subsurface reaction in the film[36].

Energetic electrons are the driving force for plasma reaction. During plasma surface interaction, some other species also form. Subsurface reaction in the films

involves many stages. The plasma species which contain both ions and neutrals are incident on the growing film[47]. Neutral species such as undissociated precursor gas, mono-radicals, di-radicals and unsaturated species contribute to the growth as the mass deposition rate exceeds the deposition rate due to ions alone. Growth rate of the film decreases with increasing temperature due to etching of the film by atomic hydrogen. Growth rate is independent of temperature but etching rate increases with temperature so the overall growth rate decreases[36].

The growth rate of the films depends on the sticking coefficient of the neutral species. Di-radicals have higher sticking coefficient of about 1 and so penetrate directly into surface bonds. Neutrals, like CH_4, have negligible effect due to low sticking coefficient.

The H ions penetrate into the film and extract H from C-H bonds forming subsurface dangling bonds. The C and H can cause subplantation. Ions in a-C:H displace H from C-H bonds and recombine with H' to form H_2 which desorbs from the film. Thus, with increasing bias voltage, H content of the a-C:H films by PECVD decreases[36].

3.2.2. Classification and Characterization

DLC is an amorphous or hydrogenated amorphous form of carbon (a-C:H) consisting of significant fraction of sp^3 and sp^2 bonds. Fraction of sp^3 bonding and hydrogen content are critical factors for the classification of DLC films. The DLC series starts from glassy and graphitic carbon to tetrahedral amorphous carbon (ta-C). Figure

3.4 is the ternary phase diagram showing composition of various forms of amorphous carbon alloys[48-50].

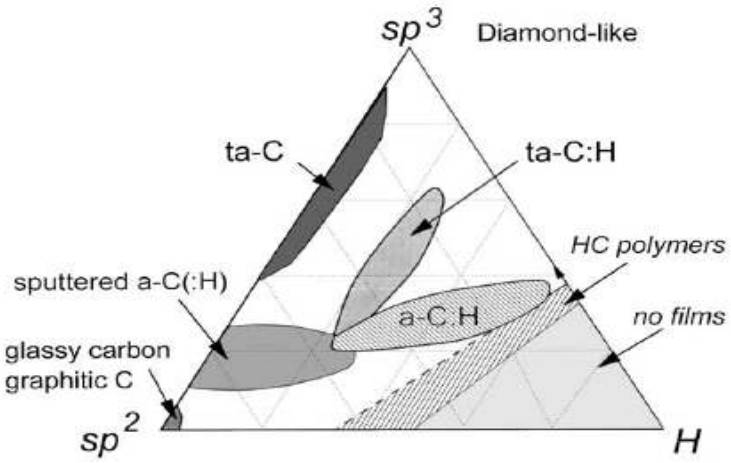

Figure 3.4 Ternary phase diagram for hydrogen free and hydrogenated amorphous carbon[48-50].

a. Classification of a-C:H films

Based on the hydrogen content and the sp^2/sp^3 ratio DLC coatings are classified into different groups[48-50]. Left hand corner of the diagram shown in Figure 3.4 represents amorphous carbon (a-C) coatings with high proportion of sp^2 bonds and unsorted graphitic structure. Relatively soft materials like soot, chars, glassy carbon and evaporated carbon are a part of this group. Hydrocarbon polymers, polyethylene $(CH_2)_n$ and polyacetylene $(CH)_n$ exist in the right hand corner of the diagram. Beyond this point no interconnecting carbon networks form and only molecules can form[36].

Sputtered hydrogenated amorphous carbon (a-C:H) is a combination of higher proportion of sp^2 bonds and lower proportion of sp^3 bonds. Predominately sp^3 bonded DLC coatings are called as tetrahedral amorphous carbon (ta-C). The interior of the phase diagram shows hydrogenated amorphous carbon (a-C:H), they have higher

content of hydrogen and lower percentage of sp^3 bonding. Deposition methods such as PECVD are used to deposit coatings with higher percentage of sp^3 bonds and lower content of hydrogen, called as tetrahedral amorphous hydrogenated carbon (ta-C:H). The properties of different states of carbon are given in Table 3.1[36].

Table 3.1 Comparison of properties of different states of carbon[36].

	Density g/cm^3	sp^3 %	H at%	Hardness GPa
Diamond	3.515	100	0	100
a-C:H hard	1.6-2.2	40	30-40	10-20
a-C:H soft	1.2-1.6	60	40-50	<10
ta-C:H	2.4	70	30	50
ta-C	3.1	80-88	0	80
Graphite	2.267	0	0	
Sputtered C	2.2	5	0	

b. Characterization techniques for bonding in amorphous carbon alloys

The sp^2/sp^3 hybridization ratio is an important parameter in characterizing the quality of DLC thin films; as the properties of the film change with this ratio[51]. The sp^2/sp^3 ratio depends on deposition conditions and technique used, hydrogen concentration and other elements in the film. Table 3.2 compares the different methods used to determine sp^3 and hydrogen content[36].

Table 3.2 Comparison of various techniques used to determine sp^3 and hydrogen content[36].

Method	Comments
NMR	Large sample needed, C^{13}, dephasing
Diffraction	Time consuming
ESCA	Small peak shifts, due to homopolar bonding
C–H modes, IR	Only sites bonded to H
ε_2/N_{eff}	OK if wide spectral range
Spectroscopic ellipsometry	Useable in situ, but small spectral range
EELS	Present method of choice, but destructive, time-consuming
Visible Raman	Indirect, sp^3 sites invisible
UV Raman	Future method of choice

Various characterization techniques such as Raman Spectroscopy, X-ray Photoelectron Spectroscopy (XPS), Nuclear Magnetic Resonance (NMR), Electron Diffraction, Electron Energy Loss Spectroscopy (EELS), Infrared Spectroscopy (IR) and Electron Spin Resonance (ESR) are used to determine these structural parameters. Each of these techniques works on different principle and is sensitive to the changes in the film structure.

3.2.3. Mechanical Properties

A major application of DLC is its use as a protective coating for various engineering fields, so mechanical properties of DLC are of fundamental interest.

a. Elastic Properties

The elastic properties of the films can be measured by using nanoindentation testing. In this experiment, the loading and unloading curve is plotted for different indentation loads and corresponding penetration depth. Figure 3.5 shows the loading-unloading curve for nano indentation measurement of a typical ta-C:H[36, 53].

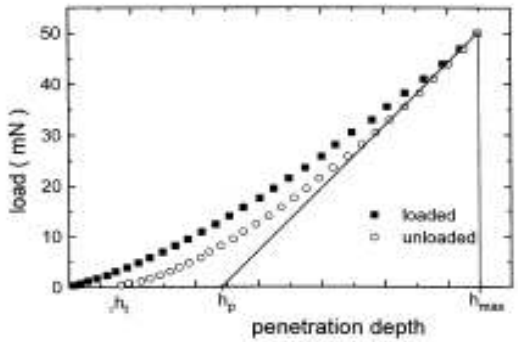

Figure 3.5 Loading-unloading curve for nano-indentation measurement of ta-C:H[36, 53]

The hardness is given by[36, 37].

$$H = 0.378 \frac{Lmax}{h^2_p}$$

and the Young's modulus is given by[36, 37]

$$E = 0.179 \frac{(1-v^2)Lmax}{(h_{max}-h_p)h_p}$$

where h_{max} is maximum indent and h_p is the plastic deformation.

The elastic properties of some DLC films are compared in Table 3.3[36, 37]. The Young's modulus of ta-C with 88% sp^3 bonding is 757 GPa, which is lower compared to Young's modulus of 1144.6 GPa for Diamond. This indicates that Young's modulus decreases with decrease in the sp^3 bonding. Whereas the Young's modulus for ta-C:H is found to be 300 GPa, which is much lower than that of Diamond and ta-C, this shows that hydrogen decrease the network co-ordination of ta-C:H[36].

Table 3.3 Elastic properties for various states of Carbon[36, 37].

	ta-C [513]	ta-C:H [513]	100% sp^3 ta-C (calculated [278,279])	Diamond
Density (g cm^{-3})	3.26	2.35	3.5	3.515
H (at.%)	0	30	0	
sp^3 (%)	88	70	100	100
Young's modulus (*E*; GPa)	757	300	822.9	1144.6
Shear modulus (*G*; GPa)	337	115	366	534.3
Bulk modulus (*B*; GPa)	334	248 (+197, −0)	365	444.8
v	0.12	0.3 (+0.09, −0)	0.124	0.07

b. Hardness

Hardness is the resistance of the material to plastic deformation. Hardness (H), Yield Stress (YS) and Young's Modulus (E) are empirically related as[36-37, 54]

$$H/Y = 0.07 + 0.06 \ln (E/Y)$$

For low Y/E ratio materials like Diamond H/Y is 1.8[42-43, 64]. According to the Orwan's approximation, yield stress is given by work done to fracture the film. In brittle materials like DLC, yield occurs by bond cleavage, so Orwan's approximation is used. $E/Y = \Pi$ and $H/E = 0.16$ for DLC[36-37, 54]

Figure 3.6 shows the variation of hardness for ta-C with sp^3 content. The hardness for ta-C increases with increase in the sp^3 content[55].

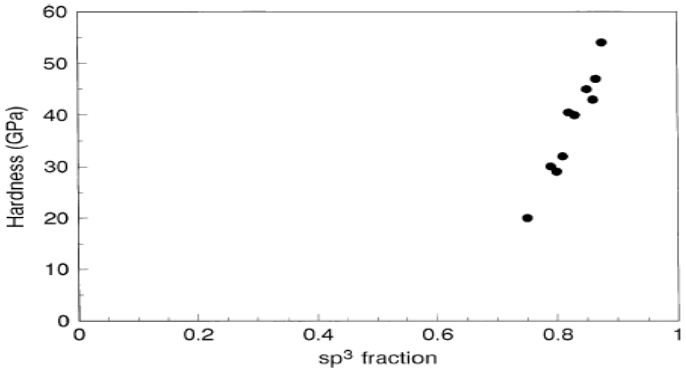

Figure 3.6 Variation of nano-hardness of ta-C with sp^3 fraction[36, 55].

c. Adhesion

DLC is used as protective coating due to its remarkable adhesive strength. To increase wear life, thick films are preferred. With the increases in film thickness, the inherent compressive stresses increase, limiting the achievable maximum thickness of the adhesive film. The film thickness (h) is related to adhesive strength (σ), surface fracture energy (γ) and Elastic modulus as[36]

$2\gamma > (\sigma^2 h / 2E)$ or $h < (4 \gamma E / \sigma^2)$

Various methods such as, use of multi layers, alloying, depositing carbide forming adhesive layers are used to reduce the internal stresses[36]. The scratch test is used to measure the adhesion strength.

d. Friction

Friction is the dissipation of energy as the two surfaces in contact move over each other. DLC has low coefficient of friction. Both intrinsic factors like degree of sp^2 and sp^3 bonding and extrinsic factors like humidity play an important role in frictional behavior[36, 43, 50]. Thus ta-C and ta-C:H behave differently.

Friction coefficient strongly depends on the humidity. The broken bonds in DLC are passivated by C-H bonds so it's inert. Diamond surface is hydrophobic, closed shell bonded system and their contact is through the weak van der Walls forces. So, when the surfaces in contact shear, the weak van der Walls forces break resulting in deformation[36].

At low humidity, when a-C:H comes in contact with the counter surface, a transfer layer of a-CH is formed. The friction coefficient in this case is low as contact is

between two hydrophobic a-CH surfaces. Higher humidity causes transfer layer to oxidize and thus hampers the formation of contact layer. So there are no van der Walls forces and transfer layer is not hydrophobic so the friction coefficient is higher[36].

e. Wear

Wear is the loss of material from the solid surface due to action of another solid. Wear depends on the applied load, at low load there is elastic contact between the surface and no wear. At moderate load, there is plastic deformation resulting in permanent groove whereas at high load, wear track shows cracking and as well as deformation[48, 50].

The wear per unit track length Q is given by Q =KA where K is the wear coefficient, a dimensionless number. It is much less than 1. A is the real contact area, which is a ratio of applied load (W) to the hardness (H). So, Q= K W/H. A dimensional wear coefficient k is defined as Q= K W/H = kW. Where k is usually given in units of $mm^3N^{-1}m^{-1}$. This shows that the wear coefficient varies inversely with the hardness, i.e., higher the hardness, lower the wear rate. The wear rate of ta-C is 10^{-9} $mm^3N^{-1}m^{-1}$ which is very low as compared to that of a-C:H 10^{-6} to 10^{-7} $mm^3N^{-1}m^{-1}$.

3.3 Cobalt-Carbon (Co-C) Nanocomposites

Co-C nanocomposites are called multifunctional as these materials show unique combination of properties i.e. mechanical, magnetic etc. Co-C thin films are used for applications such as ultra high density magnetic recording media where carbon encapsulation of cobalt weakens the exchange coupling between the magnetic domains

by increasing the effective distance between magnetic particles[57-58]. It also plays an important role in reducing media noise and preventing surface oxidation.

3.3.1 Deposition Techniques

Co- C nanocomposites can be synthesized by various techniques such as

a. Ion Beam Sputtering and Magnetron Sputtering [59-63]
b. Standard Carbon Arc [64-66]
c. Tungsten Arc Technology [67]
d. rf Magnetron Sputtering [68-69]
e. Pulsed Filtered Vacuum Arc Deposition [70]
f. Dual Electron Beam Evaporation

3.3.2. Co-C Nanocomposite Structure

Bulk elemental Co exists in two stable forms, as HCP (α-Co) structure below 425^{o}C and FCC (β-Co) structure at higher temperatures. Recently, Sun and Murray reported a third phase of elemental Co, i.e., ε-Co which has a complex cubic symmetry[1, 71]. The structure and morphology of Co-C nanocomposites depends significantly on the deposition method, deposition conditions and annealing temperature. Reports on the study of Co-C nanocomposites structural changes with annealing are summarized here

a. Nanocomposite Co-C thin films were deposited by filtered vacuum arc deposition technique and were studied for their structural changes with annealing[72]. TEM, Differential Scanning Calorimetry and XRD revealed that 60 at % Co-C nanocomposite showed amorphous structure in as-deposited condition. On annealing at 350^{o}C (metastable condition) cobalt carbide and HCP-Co formed.

Further annealing at 350-400^{o}C cobalt carbide decomposed and the structure showed HCP-Co nanocrystalline grains encapsulated by graphite like carbon[72].

b. Properties of Co-C films deposited using Co and C target by rf magnetron sputtering were investigated. Based on XRD studies, formation of amorphous like Co_xC FCC films at a substrate temperature of 150^{o}C, crystalline Co_xC film at 350^{o}C and an unidentified crystalline phase at 300^{o}C were reported[73].

c. C/Co/C granular thin films were deposited by magnetron sputtering and were explored for their structural properties. XRD studies demonstrated partially formed HCP-Co crystalline phase in as-deposited films whereas on annealing at 400^{o}C more HCP-Co crystallites were formed[74].

d. Co nanocrystals embedded in an amorphous carbon matrix were synthesized by co-deposition of Co and C using dual electron beam evaporation technique[1]. Two different films with 63 at % Co and 50 at % Co were annealed at different temperatures and were examined for their structural and magnetic properties. On basis of TEM analysis, it was reported that both the as deposited films consist of metallic ε-Co embedded in amorphous carbon matrix. On annealing at 360^{o}C, Co-C thin film with 63 at % Co showed phase transformation for Cot from ε-Co to HCP-Co, whereas the Co-C thin film with 63 at % Co transformed from ε-Co to stable FCC-Co[1].

3.3.3. Magnetic Properties

The structure of Co-C nanocomposites changes on annealing followed by a subsequent change in magnetic properties. The effect of annealing on the magnetic properties of Co-C nanocomposite is discussed here.

a. The effect of annealing temperature and the carbon content on the magnetic properties of the cobalt carbide films were investigated by Tajima and Hirano[73]. The shape of the hysteresis loop and the magnetic properties changed with the substrate temperature. At 150^{o}C, magnetization was observed to vary linearly with the magnetic field. The saturation magnetization of 100 e.m.u. per gram at 200 Oe magnetic filed and 40 Oe coercivity were reported. At 350^{o}C, the saturation magnetization was found to be 150 e.m.u. per gram at 200 Oe magnetic field and coercivity of 100 Oe. Increase in magnetization and coercivity at 300^{o}C were the result of magneto-volume effect by the interstitial carbon. At 350^{o}C, formation of an unknown non magnetic phase was reported which contributed to decrease in saturation magnetization. The increase in coercivity to maximum at this temperature was attributed to interaction between the magnetic phase and the non magnetic phase[73].

b. The dependence of in plane coercivity (H_c) and saturation magnetization (M_s) of Co-C thin films on annealing temperature were investigated by Sun et al[75]. The magnetic properties of the as deposited films and films annealed at 200^{o}C, 300^{o}C, 400^{o}C and 500^{o}C were studied. Initially, the coercivity increased with annealing temperature till it reached maximum at 400^{o}C and then decreased for films annealed

at 500^{o}C. Saturation magnetization showed linear increase with respect to the annealing temperature. M_s is a function of crystallinity of Co. Lower M_s in as deposited film and film annealed at 200^{o}C was attributed to the amorphous nature of the film. Local atomic order of Co increases with increasing annealing temperature. Increase in crystallization of Co lead to further increase in M_s at 300^{o}C. Maximum H_c and higher M_s at 400^{o}C was the result of grain coalescence and grain growth at elevated temperature[75].

c. The dependence of the in plane coercivity (H_c) and squareness ratio S= M_r/M_s on Co layer thickness of as-deposited and annealed Co-C films were investigated[74]. The graph for coercivity as function of Co magnetic layer thickness revealed, increase in H_c with respect to increase in Co thickness initially and gradually H_c decreased with further increase in Co thickness. H_c of annealed film was more with respect to as deposited film in the range of 19 to 34 nm of Co thickness, suggesting segregation of more C atoms at the Co grain boundaries and improving HCP texture of magnetic grains. For the rest of the thickness range both as deposited and annealed film followed the same trend. Squareness ratio for as deposited films did not change significantly with Co layer thickness but for annealed films it increased significantly with Co layer thickness upto 17 nm, which was attributed to in plane texture[74].

d. Co nano-crystalline embedded in amorphous carbon matrix was synthesized and studied for magnetic properties. Magnetization and magnetic field (M-H) hysteresis loop for a film with 63% Co showed saturation magnetization of 560 emu/cm^3 and coercivity of 50 Oe at 10 K. At 300 K the sample showed a decrease in the magnetic

properties with saturation magnetization of 435 emu/cm^3 and coercivity of 30 Oe. Higher coercivity suggests that even at a higher temperature, the sample was in ferromagnetic state. The ferromagnetic state is contributed to the coupling effects. The hystersis loop for film with 50 % Co showed saturation magnetization of 63.3 emu/cm^3 annealed at 300^o K coercivity of about 51 Oe at 10K, while at 300 ^{o} k it was almost zero. Coercivity of zero indicated that Co in thin films was in superparamagnetic state. The results were consistent for both zero field cooled and field cooled magnetization curves[1].

3.3.4. Co-a-C:H Nanocomposites

DLC (a-C:H) films possesses better tribological, mechanical and chemical properties as compared to C films so, replacing C with DLC in Co-C nanocomposites broadens their field of application. Recently, Co nanoparticles encapsulated in non magnetic a-C:H matrix have been attracting special attention by investigators[76]. Chua et al. synthesized a series of Co containing tetrahedral amorphous carbon (ta-C:Co) thin films under various bias conditions by an off-plane double bend Filtered Cathodic Vacuum Arc deposition technique[77]. They investigated microstructural and surface properties of ta-C:Co thin films using XPS, Raman and surface energy measurements. Their studies showed that with increasing percentage of Co in the films, the C sp^3 content decreases and with increase in bias voltage the C sp^2 content increases[77].

Laurent et al deposited films in which Co clusters were dispersed in a polymeric matrix[13, 14]. They studied the microstructural evolution and magnetic properties of the films with respect to the percentage of Co. They reported that, the film showed

superparamagnetic property below 25% Co volume fraction and ferromagnetic property above that. Their studies discuss various synthesis methods used for Co-DLC, their electrical properties, magnetic properties and surface energy, but the detailed study of the morphology and microstructural evolution of Co-DLC nanocomposites was reported by Wang and Meletis[15-17, 37].

Co-DLC nanocomposite films were deposited using a PECVD/PVD method. The films were annealed at 250^{o}C, 300^{o}C, 350^{o}C and 500^{o}C in order to study the microstructural evolution of films with respect to the annealing temperature. The TEM analysis of as-deposited films showed Co nanodots in DLC matrix. The d spacing of 2.1, 1.6 and 1.2 Å corresponded to ε-Co structure and central halo region corresponded to the hexagonal plane of defected sp^2 bonded C[15-17, 37].

The TEM analysis of films annealed at 300^{o}C showed inhomogeneous contrast, as compared to the homogenous contrast in the as deposited sample. The SAED patterns showed diffraction rings corresponding to the lattice spacing of ε-Co and orthorhombic δ'-Co_2C. The SAED for films annealed at 350^{o}C showed sharp diffraction pattern indicative of the crystalline structure. The ε-Co transformed to HCP-Co fully, upon annealing at 350^{o}C. The electron diffraction demonstrated the presence of δ'-Co_2C and HCP-Co. On further annealing at 500^{o}C, diffraction rings corresponding to δ'-Co_2C became weak, suggesting a reduction in the amount of δ'-Co_2C. The diffraction pattern showed four diffraction rings corresponding to the lattice spacing of HCP-Co. So, HCP-Co and graphite co exist at this stage[15-17, 37].

These studies demonstrated that, the structure of Co in Co-DLC nanocomposites changes on annealing, and the results are in good agreement with the previously reported studies on Co-C thin films. The research on Co-C thin films also demonstrated that, annealing can be used to tailor the magnetic properties of Co-C thin films[1, 45-47], but there is no such report on the effect of annealing on the magnetic properties of Co-DLC nanocomposites. So, we aim here to deposit and characterize Co-DLC nanocomposites with reference to previously reported studies and systematically investigate the effect of annealing temperature and microstructural evolution on the magnetic properties of these nanocomposites. Finally, we plan to follow this route and apply it to explore synthesis of Co-DLC shelled nanoparticles.

CHAPTER 4

EXPERIMANTAL PROCEDURE

4.1 Experimental Set Up

Co-DLC nanocomposites were deposited in the Surface and Nano Engineering Laboratory using a multi purpose deposition system. The system is capable of both PECVD and PVD by magnetron sputter deposition, simultaneously. Figure 4.1 shows schematic representation of the deposition system.

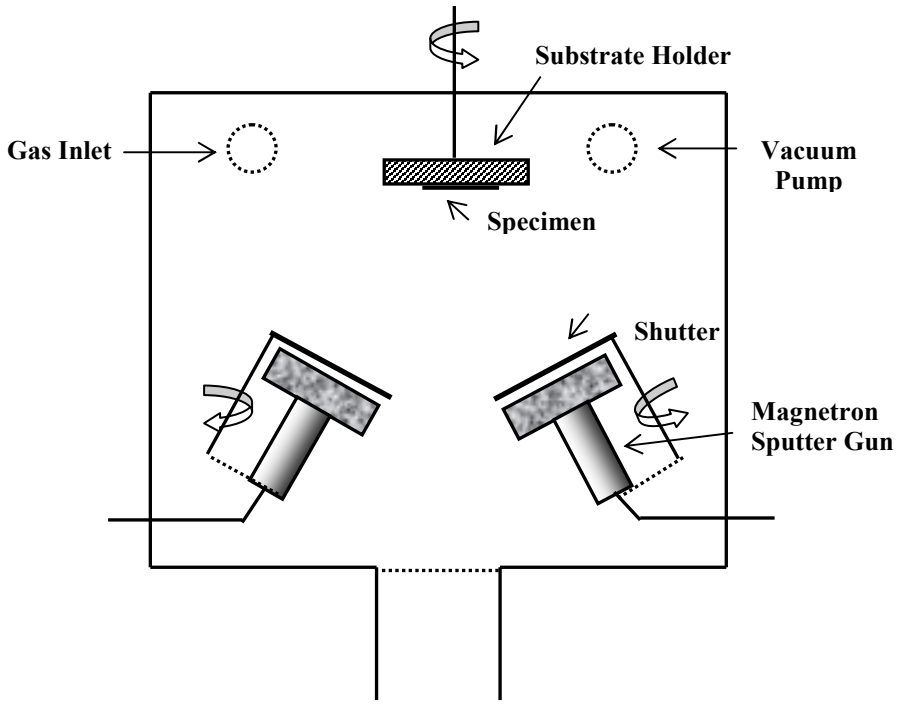

Figure 4.1 Schematic of the deposition system.

The deposition system consists of a cylindrical stainless steel chamber, specimen holder with rotation, heating and bias capabilities and various ports

supporting two magnetrons, a baretron and an automatic gate valve. The two DC/RF magnetrons can hold 2" diameter targets of 0.125" to 0.25" thickness. The two magnetrons are equipped with shutters which can be used for single or dual deposition. Different gases can be introduced into the chamber and the gas flow rate can be controlled via a gas controller. Various films can thus be deposited by controlling the gas flow rate, pressure and bias.

4.2 Deposition of Co-DLC Nanocomposites

Co-DLC nanocomposites were deposited on Si (001) substrate by the above mentioned hybrid PECVD/PVD technique. Before deposition, the Si substrate holder was cleaned with methanol and the chamber was evacuated down to pressure of $1x10^{-6}$ Torr. The chamber was purged with argon several times to clean the environment. The sample was then sputtered cleaned using Ar^+ at 25 mTorr pressure and bias voltage of -1000 V for 10 min.

Co-DLC films were synthesized by incorporating Co via sputtering of pure Co target (99.96% pure) using current control. After sputter cleaning of the target, methane was introduced into the chamber and the CH_4/Ar ratio was fixed at predefined values. The substrate was biased at -500 V and the magnetron current was set to 120 mA. The substrate rotation was set at 20 rpm and while the magnetron was cooled with water continuously. Thus, a series of Co-DLC nanocomposites were deposited by varying CH_4/Ar gas ratio or different pressure that ranged from 25 mTorr to 50 mTorr. After deposition the sample was cooled inside the chamber in presence of argon.

4.3 Characterization of Co-DLC Nanocomposites

4.3.1 Composition

Composition of the nanocomposites was measured using Energy Dispersive Spectroscopy (EDS) in conjunction with Scanning Electron Microscopy (SEM), JEOL, JSM-6100. The characterization was carried out at 10 keV acceleration voltage and beam current of 200 μA.

4.3.2 Thickness and Roughness

The thickness and roughness was measured using Wyko Surface Profiler. The surface profiler was operated under PSI mode and surface data, 3-Dimensionnal interactive display and x and y profiles for thickness and roughness were captured for all the samples. The deposition rate was calculated based on the thickness of the film and time of deposition.

4.3.3 Transmission Electron Microscopy (TEM)

Plan view and cross section TEM samples were prepared for characterizing the microstructure and structure of the phases present. Cross section TEM samples were prepared using the following steps,

a. A small square section of the sample was cut using a diamond knife and was glued on the holder with thin film side facing the holder.
b. Two rectangular sections with size 3mm x 1mm were cut from the sample on an Isomet low speed saw.

c. Two small sections were removed from the holder and cleaned with acetone. The two sections, with thin film facing each other were glued with M Bond 610 adhesive. The sample was placed on the holder and heated for 20 minutes at 150^{o}C.

d. The sample was glued on the holder and grinded on an Ecomet variable speed grinder polisher at 120 rpm with three different diamond lapping paper size 6 μm, 3 μm and 0.1 μm respectively. The sample was ground till shiny surface was produced and all scratches were removed. The sample was removed from the holder and washed with acetone.

e. The thin film side of the sample was glued with the shiny side on copper grid with M Bond 610 adhesive. The sample was kept at the center of the copper grid and heated for 20 minutes at 150^{o}C.

f. The sample was polished on the 600 grit polishing paper using distilled water. The sample was polished till its thickness reached 120 μm.

g. The sample was mounted on the Dimple grinder 656 and was aligned with the microscope. The sample was dimple ground with brass wheel using 3 micron diamond paste as a lubricant. The sample was further ground with stainless steel wheel using alumina paste as the lubricant and was then cleaned with acetone.

h. The sample was mounted on the precision ion milling system for ion milling. The pressure was set to 5 x 10^{-2} Torr with the stage rotation at 4 rpm. The sample was kept for ion milling till there was a small hole in the sample.

i. The sample was inspected under a Nikon Eclipse ME600 optical microscope. The sample was then ready for TEM analysis.

The TEM sample was mounted on a JEOL JEM-1200EX TEM operated at an acceleration voltage of at 120 keV. The images were taken at different magnifications ranging from 100K to 300K. Also selected area electron diffraction patterns were taken for structural analysis.

4.3.4 X-Ray Photoelectron Spectroscopy (XPS)

The properties of the Co-DLC nanocomposites depend on the sp^3/sp^2 ratio of C bonds. The XPS can provide the percentage of sp^3 and sp^2 C-C and C-H bonding. Hydrogen cannot be detected using XPS so this technique does not give percentage of hydrogen present. Table 4.1 gives the binding energies and the type of bond present for C1s peak[43]. The C1s high-resolution spectrum can typically be deconvoluted into four different peaks as Co-C peak at 283.5 eV, C-O peak at 286.5 eV, sp^3 C-C and C-H peak at 284.8 eV and sp^2 peak at 284.3 eV. The percentage of individual bond type can be calculated by measuring the area under the peak.

Chemical state analysis was carried out using a Perkin Elmer digital 500 XPS. The base pressure used was 5×10^{-9} Torr. Aluminum at 300 W was used as the X-ray source. The survey spectrum was acquired with binding energy ranging from 0 eV to 1200 eV, with an increment of 0.025 eV per step. Ten sweeps were acquired for each spectrum. The pass energy used was 8.95 eV.

Table 4.1 Binding energies for C 1s electrons[37].

Material	Binding energy (eV)	Chemical bond
a-C:H	284.3	C-C sp^2 or C_6H_6
(Polymer-like,	285	C-C sp^3 or $-CH_3$
Diamond-like, Middle)	286.4	C-O
	287.7	C=O
	289.1	O-C=O
a-C:H	284.4-284.75	
a-C:H	284.3	sp^2
	284.8	sp^3
	286.1	C=O
a-C	284.3±0.1	sp^2
	285.2±0.1	sp^3
Graphite	284.36, 285.6	sp^2
Diamond	285.35, 290.45	sp^3
Co/C multilayer	283.2	C-Co (i.e., carbide)
	284.1	C-C (graphite)
Co-polymer	284.6	C-C, C-H
	286.2	C-O-C, C-OH
	288.2	O-C=O
$Co_{65}C_{35}$ film	283.5/283.1	C-Co (carbide)
	284.1	C-C

The survey spectrum was analyzed and the peaks were identified for major elements present. High resolution spectra for C and Co were acquired for further investigation of the sp^3/sp^2 ratio. Spectrum analysis and deconvolution of the high resolution spectra of C was carried out using the Casa XPS software. The percentage of sp^3 and sp^2 bonds and their ratio in the C 1s high resolution peak were calculated.

4.3.5 Fourier Transformed Infrared Spectrometry (FTIR)

A Thermo Electron Corporation Nicolet 6700 FTIR was used to study the percentage of hydrogen bonding present in the nanocomposites. The FT-IR spectrum was acquired for both Si wafer and nanocomposite in the wavenumber range of 400-4000 cm^{-1} in the absorbance mode. The spectrum for Si was subtracted from the spectrum for nanocomposites for further analysis. The peaks were identified for C-H stretching bonds. The C-H bonds were further deconvoluted to calculate the percentage of C-H sp^3 and sp^2 bonds present in the nanocomposites.

4.4 Mechanical Testing

Indentation experiments were performed on a Leco LM 300 AT Microhardness Tester. The micro indentations were taken with the Knoop diamond indenter and the load applied was 25 g_f. Five readings per sample were taken down and the Knoop hardness number was calculated using the formula,

$$KHN = F / A = P / CL^2$$

where, KHN is Knoop hardness number

A is the unrecovered projected area of the indentation in mm^2

F is applied load in kg_f

L is the length of long diagonal in mm

C is a constant of the indenter relating projected area of indentation to the square length of the length of the long diagonal. C is equal to 0.07028.

The Knoop hardness number was then converted to hardness in terms of Kg/mm^2 using standard charts.

4.5 Tribological Testing

Tribological properties, i.e, wear rate and coefficient of friction, for Co-DLC nanocomposites were investigated by conducting pin-on-disc testing using a CSM computer controlled Tribometer. The test was performed using 1 N load with sliding distance of 1000 m and sliding velocity of 10 cm/s. An Al_2O_3 pin with diameter 9.5 mm was used for the test. The coefficient of friction was recorded as a function of sliding distance.

The wear track profile was acquired using the Wyko Surface Profiler. The wear rate was calculated using the formula

$$W = V/ (LS)$$

Where W is the average wear rate, V is the volume of the material removed, L is the applied load and S is the sliding distance.

4.6 Magnetic Properties

The Micromag™ 2900 Alternating Gradient Magnetometer (AGM) was used for the magnetic properties measurement. The probe was calibrated before starting the experiment. A sample with size 3 mm x 3 mm was cut with a diamond knife and inserted into the magnetometer. Hystersis loop was acquired, for both in plane and out of plane magnetic field applied to the surface of the sample. The hystersis loop was normalized with respect to the volume of the sample.

4.7 Annealing Experiments

The microstructure of the Co-DLC nanocomposites changes on annealing. As reported by previous studies, the as deposited Co-DLC films consist of defected

metallic ε-Co embedded in an amorphous carbon matrix. Annealing at 250^{o}C films produced no change in the structure but the crystallinity was enhanced by annihilation of defects. On further annealing at 360^{o}C, Co-C thin films showed a phase transformation for Co from ε-Co to HCP-Co and the amorphous carbon transforms to graphite[1].

Based on the previous studies, experiments involved annealing of selected nanocomposites at 250^{o}C and 500^{o}C for 2 hours. The samples were annealed in vacuum at 10^{-6} Torr in the deposition system. Samples were cooled in an Ar atmosphere in the vacuum system after annealing.

To study the effect of annealing on chemical states of C 1s electron, high resolution spectra for selected nanocomposite annealed at 250^{o}C were acquired. The spectra were further deconvoluted to determine the percentage of sp^3 and sp^2 bonding.

Magnetic property measurements were conducted for selected samples annealed at 250^{o}C and 500^{o}C. Hystersis loops were acquired for the samples with both in plane and out of plane magnetic field applied to the surface of the sample.

4.8 Shelled Co/DLC Nanoparticles

After characterization and careful analysis of all nanocomposites, one nanocomposite with the best combination of magnetic, tribological, and mechanical properties, was selected for fabrication of shelled Co/DLC nanoparticles. A thin film of about 20 nm of the selected nanocomposite was deposited on a carbon coated copper grid. The thin film was deposited at 35 mTorr pressure and Ar/CH_4 ratio of 4.3, with

magnetron current of 120 mA. Subsequently the copper grid was used for TEM analysis to investigate the structure of the film.

The procedure for deposition of the thin film for making shelled Co/DLC nanoparticles was as follows. Si wafer with (001) orientation was used as the substrate. Polystyrene particles with 100 nm size were used as mask. The surface of the substrate was functionalized to develop a positive charge. The polystyrene particles were deposited on the Si substrate by Nanosphere Lithography. The Si wafer with the polystyrene particles was loaded on the substrate holder of the deposition chamber. Using the same deposition conditions as used for the film on the copper grid, a thin film of about 20 nm was deposited on the polystyrene particles in the PECVD/PVD system. Initially, only DLC was deposited for 3 minutes (no magnetron sputtering), to obtain 5 nm thin DLC film. The magnetron was then turned on and Co-DLC deposition was conducted for next 6 minutes, to deposit 10 nm Co-DLC thin film, followed by deposition of pure DLC (no magnetron sputtering) for 3 minutes (5 nm DLC layer). The aim here was to encapsulate Co nanoparticles by the DLC matrix. The sample was cooled inside the chamber.

Based on the results of the previous section, 6 minutes deposition of Co-DLC at the above conditions is expected to produce 10 nm thin Co-DLC films sandwiched in 5 nm of DLC on both the side. The sample was immersed in toluene, to dissolve the polystyrene particles and release the Co-DLC particles deposited on them. The solution was placed on top of a magnet for 24 hours, to collect all the particles at the bottom of the vial. Subsequently, most of the solution was removed from the vial and the rest was

kept on the magnet for next 10 hours. Then, the vial was removed from the magnet and a drop of solution from the bottom of the vial was put on a copper grid and allowed to dry. Subsequently, the copper grid was analyzed with TEM.

CHAPTER 5

RESULTS AND DISCUSSION

5.1 Deposition of Nanocomposites and Effect of Processing Parameters

A series of nanocomposites with different processing parameters were deposited. Among all the nanocomposites, six of them were identified for further investigation based on their characteristics. Table 5.1 presents the processing parameters and composition of the selected nanocomposites. All nanocomposites were deposited at the same applied bias voltage of -500 V, magnetron current of 120 mA, substrate rotation of 20 rpm. Their composition was obtained by EDS analysis. Five measurements were conducted for each sample to validate the results. The results show that pressure and Ar/CH_4 ratio can be used to control the composition of the nanocomposites.

Table 5.1 Processing parameters and composition for the selected nanocomposites.

Nanocomposites	**Pressure (mTorr)**	**Ar/CH_4 Ratio**	**Co At %**	**C At %**
Nanocomposite 2	25	4.3	74.73	25.27
Nanocomposite 7	30	4.3	64.89	35.11
Nanocomposite 4	35	4.3	49.74	49.46
Nanocomposite 5	40	4.3	24.12	75.98
Nanocomposite 6	30	13	78.39	21.61
Nanocomposite 8	35	13	59.65	40.35

Figure 5.1 illustrates that as the chamber pressure increases the percentage of Co in nanocomposites decreases whereas, percentage of carbon increases. With increase

in pressure, the ionization in the plasma decreases along with the energy of sputtering species (Ar^+ and CH_4^+). Thus, at higher pressure the sputtering rate of the Co target decreases reducing the Co content in the film. At the same time at higher pressure, larger hydrocarbon fluxes reach the substrate resulting in the direct DLC deposition and thus, lower Co content. This is in agreement with previous studies on Me-DLC, which report that as the pressure increases the metal content in the film also increases[52].

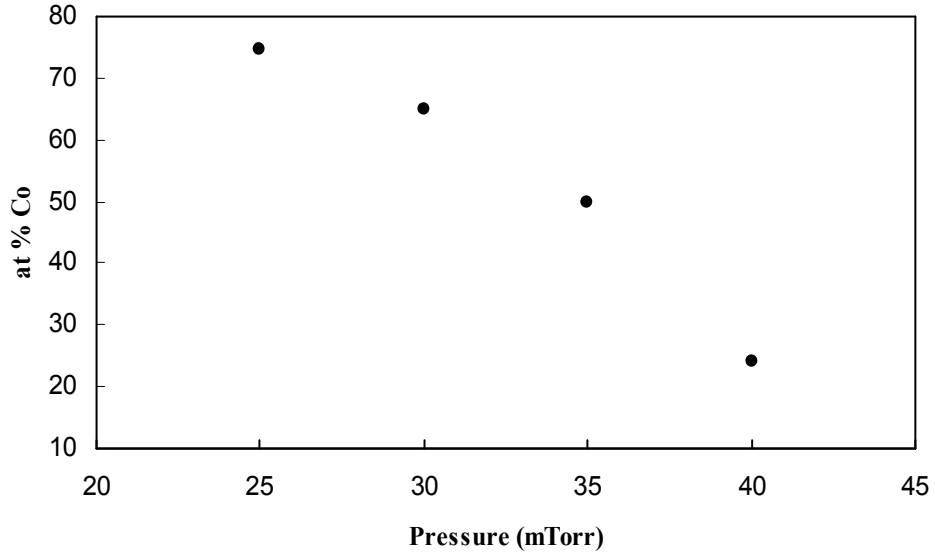

Figure 5.1 The effect of pressure on Co content in the Co-DLC nanocomposite films.

Furthermore, as Ar/CH_4 ratio is increased from 4.3 to 13, the percentage of Co increases. Ionization efficiency of Ar is high, so higher Ar content in the precursor gas results in higher plasma density and thus higher sputtering yield resulting in higher Co content in the film. The nanocomposites with the precursor Ar/CH_4 gas ratio of 13 were eliminated from the study. As the Ar content increases, the percentage of Co increases but at the same time higher content of Ar may cause surface sputtering of the growing

film resulting in lower hardness. Previous studies showed that at higher Ar/CH_4 ratio, the primary species for deposition is C_2 whereas at lower Ar/CH_4 ratios, CH_3 is the dominating species leading to the deposition of a-C:H films[39].

5.2 Thickness and Roughness

Thickness and roughness for selected nanocomposites was measured using a Wyko profiler. Thickness and roughness measurements were taken at different locations of the sample to obtain valid values. As per Table 5.2, the deposition rate increases with increase in pressure.

Table 5.2 Thickness, roughness and deposition rate for Co-DLC nanocomposites.

Nanocomposites	**Pressure (mTorr)**	**Co at %**	**Thickness (nm)**	**Roughness (nm)**	**Deposition Rate (nm/min)**
Nanocomposite 2	25	74.73	91.3	1	1.52
Nanocomposite 7	30	64.89	108	1.2	1.8
Nanocomposite 4	35	49.74	117	1.5	1.95
Nanocomposite 5	40	24.12	184	1.7	3.06

The roughness of all nanocomposites is nearly the same, ranging from 1 nm to 1.7 nm, indicating that there is no effect on the surface at the selected processing conditions range. Figures 5.3 (a) and 5.3 (b) show the three dimensional interactive display representative roughness and roughness profile respectively, corresponding to Nanocomposite 4.

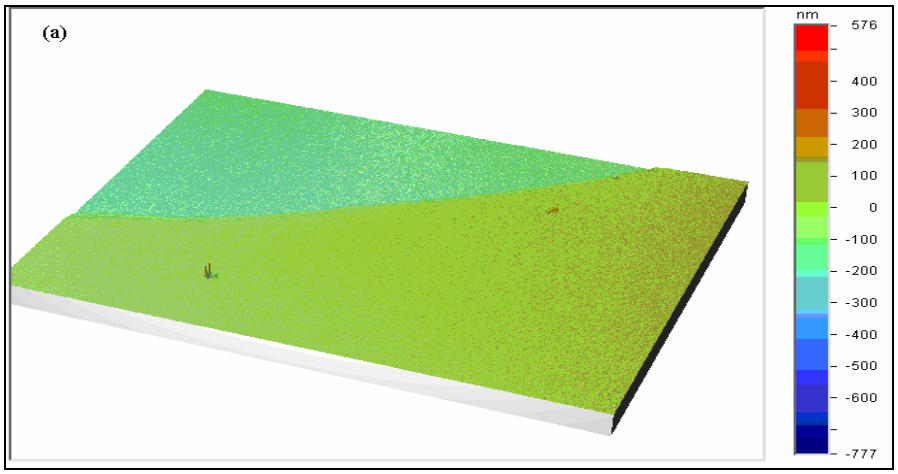

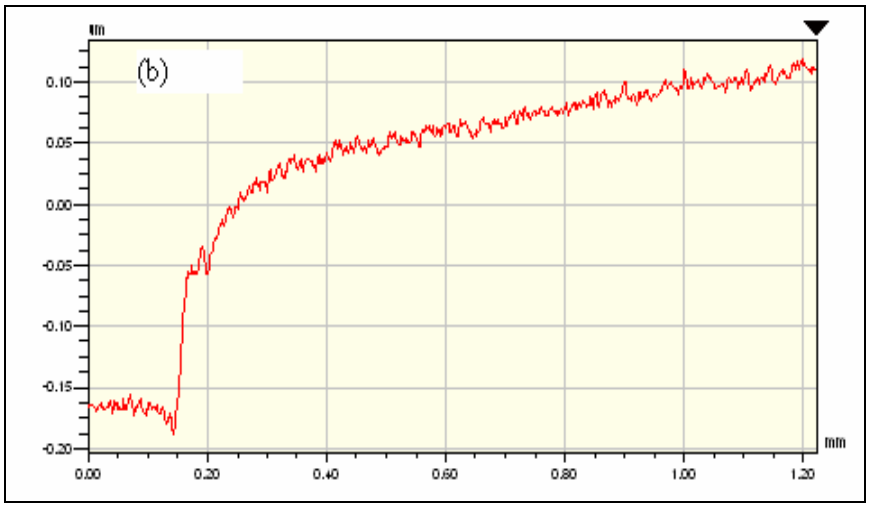

Figure 5.2 (a) Thickness three dimensional display and (b) Thickness profile for Nanocomposite 4.

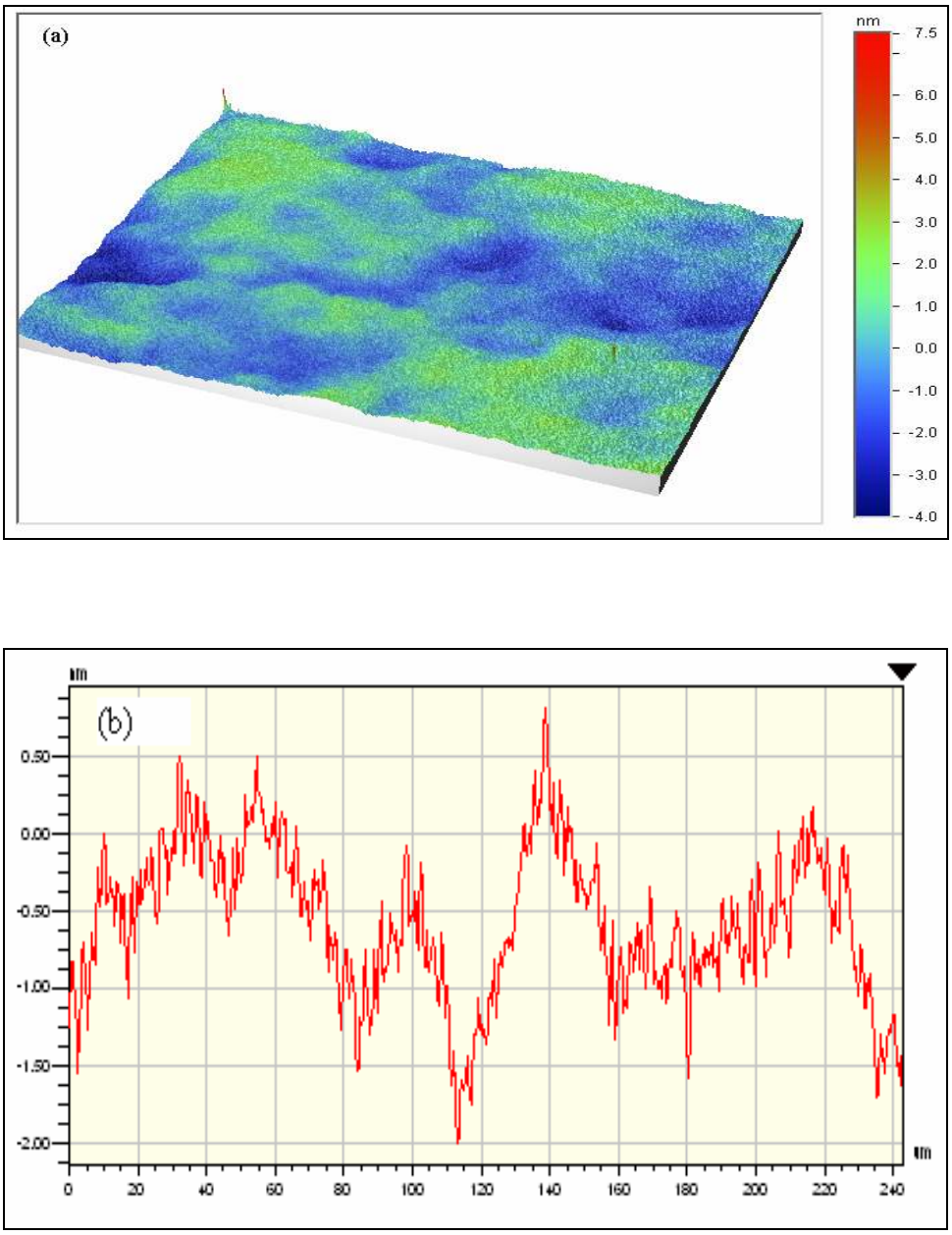

Figure 5.3 (a) Roughness three dimensional display and (b) Roughness profile for Nanocomposite 4.

The deposition rate was calculated from the film thickness and deposition time. All films were deposited for one hour. The highest deposition rate was found to be 3.06 nm/min obtained at 40 mTorr pressure for Nanocomposite 5. This indicates that the

deposition rate increases with the increase in the pressure. At higher pressure, the deposition rate increases due to higher hydrocarbon flux reaching the surface.

5.3 TEM Analysis

Plan view and cross sectional TEM observations were made to characterize the three dimensional microstructure of the nanocomposites. SADP was utilized to identify the crystal structure of the phases present. Figures 5.4 (a) and (b) show cross sectional images of Co-DLC Nanocomposite 4 and 7, respectively. The cross sectional TEM micrographs show the Co-DLC film, Si substrate and the film substrate interface. The long, dark, columnar substructure represents Co nanocolumns, whereas the bright region corresponds to the DLC matrix.

For Nanocomposite 4, the lateral size of the nanocolumn ranges from 10 to 18 nm. The dark columnar structures grow continuously from the interface to the top surface of the film. The length of the column in this nanocomposite is equal to the thickness of the nanocomposite (116 nm). So, in this case, the columns have an aspect ratio of about 8.2. The intercolumnar distance is about 2-4 nm, indicating that the columns are encapsulated by DLC matrix. The nanocolumns in Nanocomposite 4, grow parallel to the growth direction of nanocomposite. This suggests that, Co nucleates at the interface and starts growing as Co nanocolumns along the entire thickness of the film.

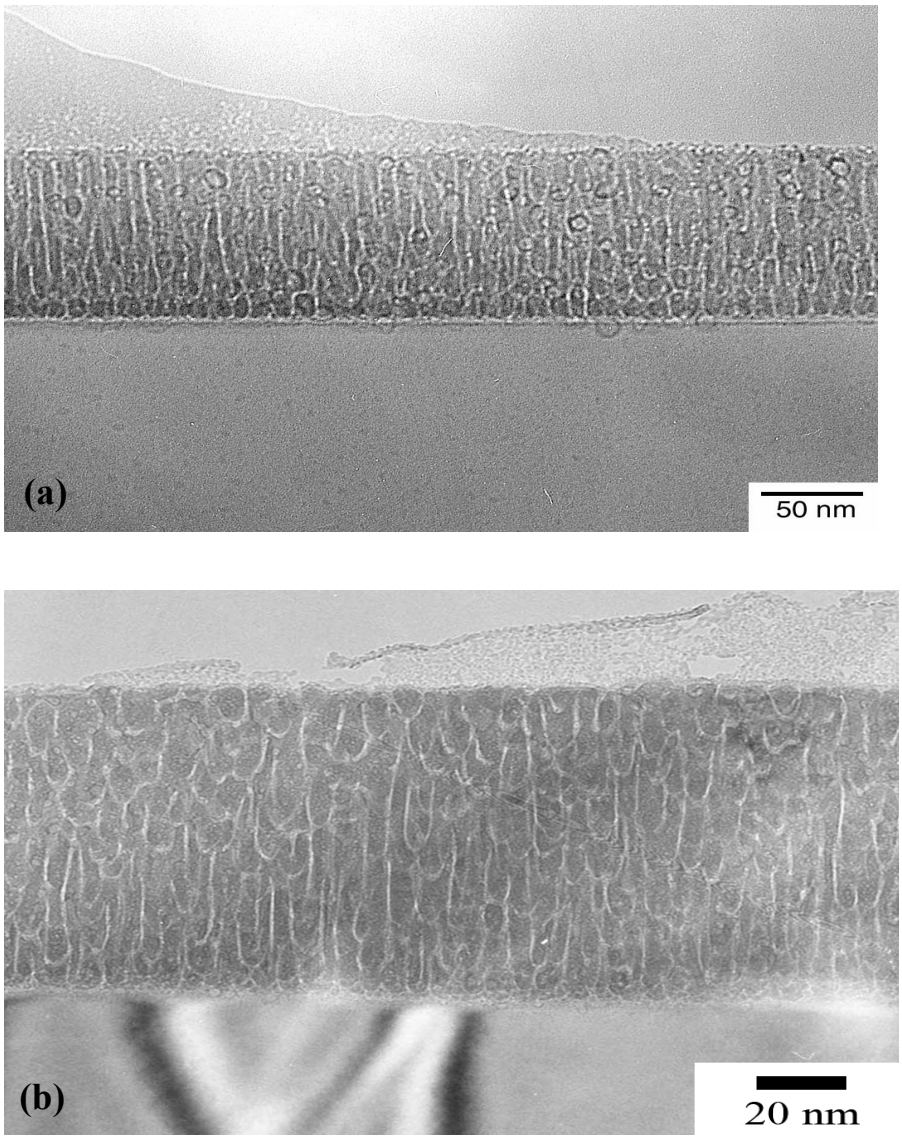

Figure 5.4 Cross sectional TEM images for Co-DLC Nanocomposites (a) 4 and (b) 7.

Cross section TEM observations of Nanocomposite 7 also show columnar structure. In this case, the nanocolumns grow laterally. With increase in the Co content the Co is accommodated by an increase in the column lateral directions. Thus, very thin DLC boundaries are produced for this film. Similar observations have been made

previously by Liu et al[79, 80]. It is important to note that these results show that formation of such nanocolumnar structure is not system dependent. Also, these results help confirm and further Co nanocolumnar characteristics.

Figures 5.5, 5.6 and 5.7 show plan view TEM images and in plane distribution of columnar structure for Nanocomposites 5, 4 and 7, respectively. The dark region represents cross section of the Co nanostructure having round shape morphology. The Co nanostructures are separated by a layer of DLC matrix, represented by bright region. The size of Co nanostructures for Nanocomposite 2 is equal to 5 to 9 nm. Majority of the nanostructure appears like isolated, single particles, surrounded by thin DLC matrix of about 4-5 nm. Occasionally, two particles merge together to form a single big particle.

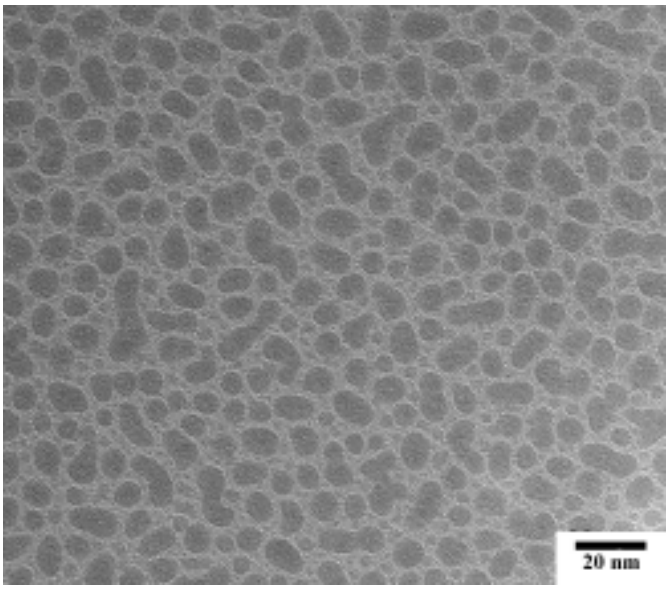

Figure 5.5 Plan view TEM image for Co-DLC Nanocomposite 5.

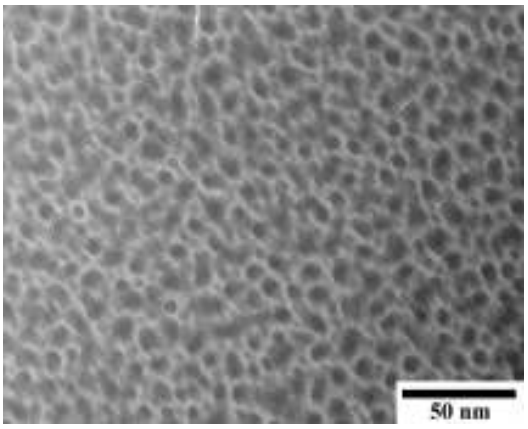

Figure 5.6 Plan view TEM image for Co-DLC Nanocomposite 4.

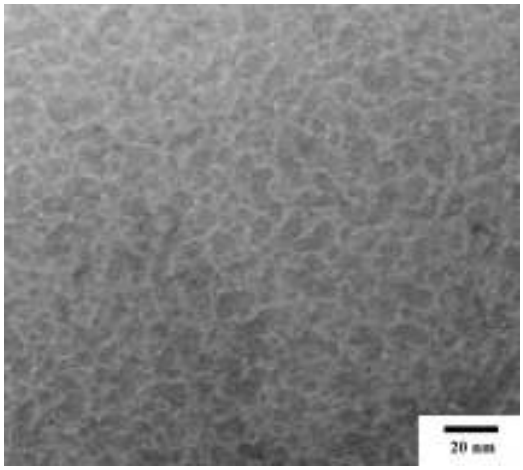

Figure 5.7 Plan view TEM image for Co-DLC Nanocomposite 7.

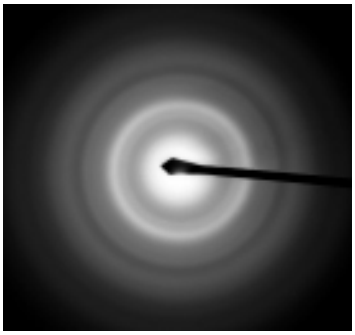

Figure 5.8 DP for Co-DLC Nanocomposite 4.

Nanocomposite 4 shows a Co nanostructure of about 10 to 18 nm surrounded by DLC matrix of around 2-3 nm. For Nanocomposite 7, the Co nanostructures agglomerate to form big size particle due to their large size. The particles are not well separated by DLC matrix. The size and morphology of the Co nanostructures is associated with the Co content in the nanocomposites.

The electron diffraction pattern for the Co-DLC Nanocomposite 4 shows five diffraction rings 1, 2, 3, 4 and 5; from center of the pattern with d spacing 0.85 Å, 1.05 Å, 1.2 Å, 1.6 Å, and 2.1 Å, respectively. The d spacing of the first four rings corresponds to (631), (522), (500), (321) of ε-Co whereas ring 5 corresponds to lattice spacing of either (200) or (300) of ε-Co. Thus, as-deposited film shows ε-Co Nanoparticles in DLC matrix. These results are in agreement with the previous studies on Co-DLC by Liu et al[79, 80] and confirm the formation of this metastable phase under these deposition conditions.

5.4 XPS Analysis

XPS is a surface analysis technique and sensitive to the top few atomic layers of the material (up to a depth of about 1 nm). The XPS technique is used to investigate the chemical composition of the thin films and the chemical states of the elements present. So the XPS technique plays a very important role in the characterization of the DLC thin films. The survey spectrum for Nanocomposite 4 and 7 mainly exhibits C and Co peaks. An insignificant amount of oxygen was detected in the films indicting the absence of Co oxide formation in the as-deposited films. Hydrogen cannot be detected by the XPS technique.

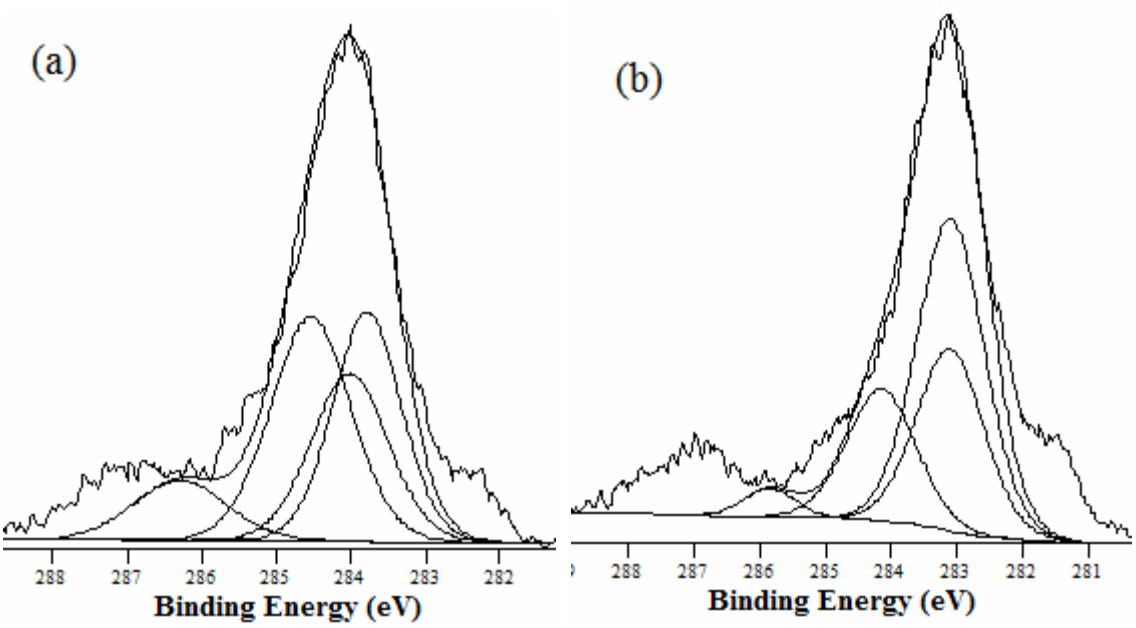

Figure 5.9 High resolution spectra for the C 1s electron for (a) Nanocomposite 4 and (b) Nanocomposite 7.

High resolution spectra were acquired for both C and Co. The high resolution spectrum of C 1s was further analyzed to determine the various chemical states present for carbon. As per Table 4.1, the C 1s can exist in different chemical states. The high resolution spectrum for C 1s was deconvoluted into four different components Co-C at 283.5 eV, sp^2 C-C/C-H bond at 284.3 eV, sp^3 C-C/C-H bond at 284.8 eV and C-O/ -CH_2O- bond at 286.5 eV. Figures 5.9 (a) and (b) illustrate the high resolution spectra for C 1s electron for Nanocomposites 4 and 7, respectively.

Table 5.3 gives the percentage of the four carbon states and overall composition of the nanocomposites. The percentage contribution of each state to C 1s electron spectrum was calculated by dividing the area under the peak of each chemical state by

the overall area of the C 1s peak. The results indicate that as the Co content increases, the percentage of sp^3 decreases while the percentage of sp^2 increases. Also, the percentage of Co-C increases with increase in the Co content. Similar trends have been observed previously not only for Co-DLC but also for other Me-DLC systems like Cr-DLC[52].

Table 5.3 Percentage of four C states and overall composition of the nanocomposites.

	Peak Position Binding Energy (eV)	**Nanocomposite 4**		**Nanocomposite 7**	
		% Conc. in C 1s Peak	**% Conc. in Nano-composite**	**% Conc. in C 1s Peak**	**% Conc. in Nano-composite**
Co_x-C	283.5	30.06	15.03	44.59	28.98
sp^2	284.3	24.74	12.37	26.36	17.13
sp^3	284.8	34.46	17.22	23.03	14.96
C-O	286.5	10.74	5.37	6.02	3.90

Decrease in the sp^3 content can be attributed to the increase in the Co content. As the Co content increases, the contribution of Co bonded carbon increases. With increases in the Co percentage; more C atoms interface Co atoms and thus, less C atoms are available for the formation of C-C or C-H bond, which leads to the decrease in the sp^3 bonds. The sp^3/sp^2 ratio for Nanocomposite 4 is higher than the ratio for Nanocomposite 7.

With increasing pressure, the sp^3 percentage in the nanocomposites increases. As pressure increases, the number of collisions in the plasma also increases resulting in medium energy flux promoting sp^3 bonding. This explains the higher percentage of sp^3

bonds in nanocomposite deposited at 35 mTorr as compared to the nanocomposite deposited at 30 mTorr. Previous studies have reported the same trend of higher sp^3 content with increasing pressure due to lower impact energy of ions by scattering[52].

The contribution of the various states of carbon in overall nanocomposite is calculated by multiplying the percentage of carbon states in the C 1s peak by the percentage of carbon present in the nanocomposite. The percentage of sp^3 bonds in the overall composition of Nanocomposite 4 is 17.22 % whereas for Nanocomposite 7 is 14.96 %. Both nanocomposites show a small presence of C-O bonds. Some residual oxygen present in the chamber can possibly be incorporated into the nanocomposites during deposition, interacting with carbon atoms forming C-O or $–CH_2O-$ bonds.

Thus, in summary as percentage of Co increases the percentage of sp^3 bonds decreases with the increase in the Co-C bonds.

5.5 FTIR Analysis

FTIR spectroscopy is commonly used to characterize C-H bonding in a-C:H films. FTIR is used for the investigation of presence of hydrogen in the nanocomposites. The FTIR spectrum was acquired for both nanocomposites and Si wafer in the absorbance mode. The spectrum for Si was subtracted from the spectrum for the Co-DLC nanocomposites.

A broad band was observed at wavelength of about 2800 to 3100 cm^{-1} indicating the relatively high hydrogen content in the film. The particular region was selected followed by baseline correction and smoothing of the spectra. The spectra were deconvoluted for the detailed analysis of C-H stretch bonds. Figures 5.10 (a) and (b)

show the deconvolution of the C-H stretch bonds for Nanocomposite 4 and 7, respectively.

Table 5.4 summarizes the various stretching modes present in the deconvoluted C-H stretching region and their relative intensities. The relative contribution of each peak is calculated by considering the area under the peak. The stretching region in this case shows mainly the presence of sp^3 C-H vibration. As reported earlier, the sp^2 in this particular region shows absorption at around 3060 cm^{-1} (aromatic) and 3000 cm^{-1} (olefinic)[78]. So, the sp^2 C-H bond present here may be associated with olenific bonds.

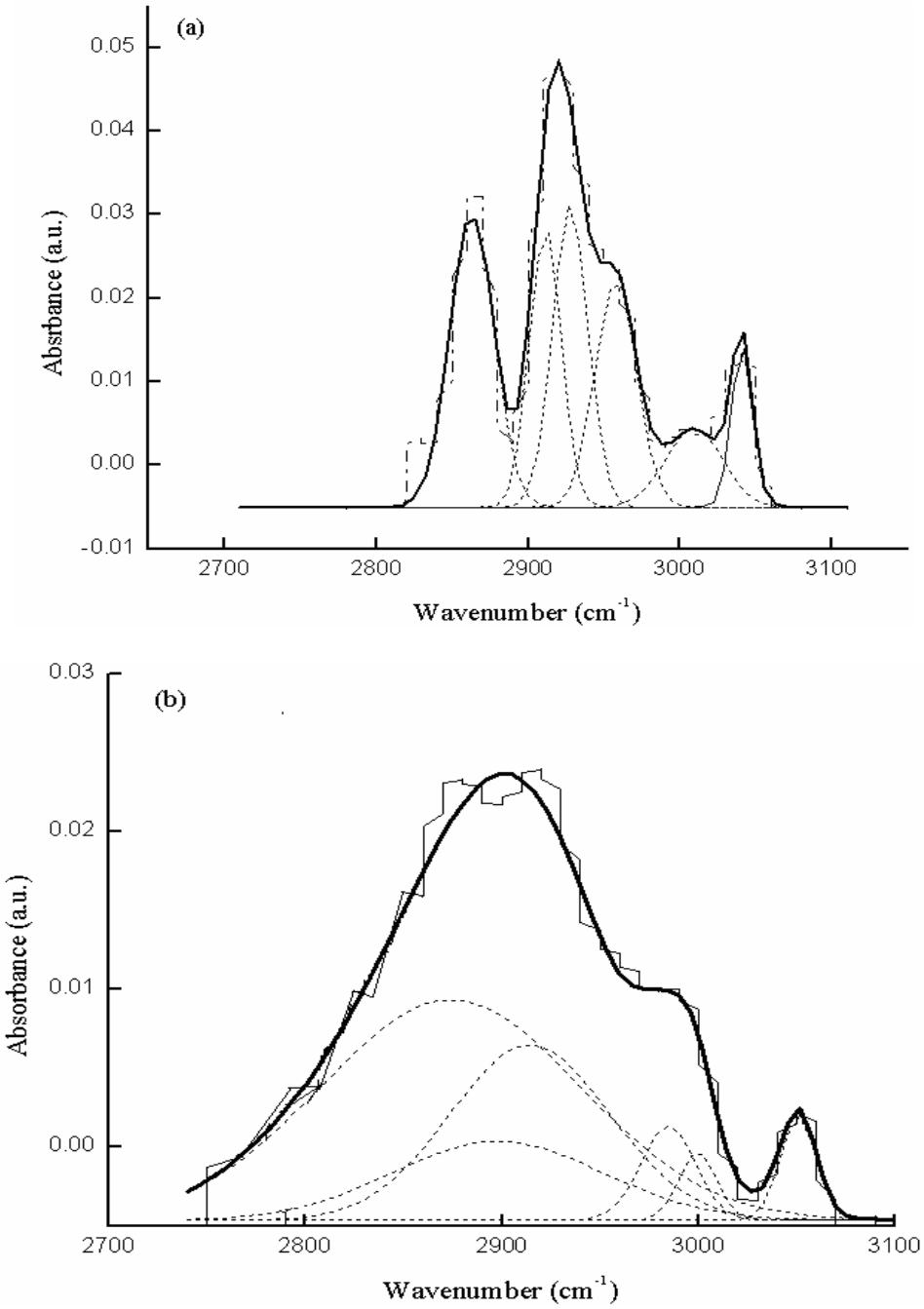

Figure 5.10 Deconvoluted FTIR spectra for C-H stretch bonds for (a) Nanocomposite 7 and (b) Nanocomposite 4.

Table 5.4 Assignment of C-H stretch bonds for Co-DLC Nanocomposites 4 and 7.

Wavenumber (cm^{-1})	**Assignment**	**Nanocomposite 4**	**Nanocomposite 7**
		Peak Contribution (%)	**Peak Contribution (%)**
2868	sp^3 C-H, $C-H_2$, $C-H_3$	50	26
2904	sp^3 $C-H_2$, C-H	14	18
2920	sp^2 (olef) $C-H_2$	25	21
2970	sp^3 $C-H_3$	4	19
3004	sp^2 (olef) C-H	3	9
3045	sp^2 (olef) $C-H_2$	4	7
Sp^3/sp^2		2.12	1.7

Table 5.4 indicates that as the percentage of Co in the nanocomposite increases the sp^3 content decreases. As percentage of Co increases the percentage of both C and hydrogen decreases leading to smaller number of sp^3 bonds. It also shows that with decrease in the percentage of sp^3 bonds the percentage of sp^2 bonds increases thus, affecting the ratio of sp^3/sp^2 bonds. The sp^3/sp^2 ratios were found to be 2.1 and 1.7 for Nanocomposites 4 and 7, respectively. This signifies that as the Co content in the film increases the hydrogen content decreases with increase in the sp^3/sp^2 ratio. This is in agreement with the XPS results reported in the previous section. Though this method provides useful information about the C-H stretch bonds it does not give the actual percentage of the hydrogen present in the Co-DLC nanocomposites.

The sp^3/sp^2 ratio given by FTIR for both Nanocomposites 4 and 7 are higher as compared to those given by the XPS analysis. The XPS results cannot be compared with the FTIR results as XPS analysis considers both C-C and C-H bonds, while FTIR

deals with C-H stretch bonds[78]. The techniques are complementary. Both XPS and FTIR analysis indicate that the percentage of C-H bonds is more than that of the percentage of C-C bonds.

5.6 Mechanical Properties

The indentation tests were carried out to assess the microhardness of the nanocomposites. Five readings were taken for each sample to obtain statistically valid results. The variation of the microhardness with Co content in the Co-DLC nanocomposites is illustrated in Figure 5.11. The microhardness for Nanocomposite 4 was found to be 11.3 GPa and that for Nanocomposite 7 was found to be 10.5 GPa. The hardness for the a-C:H hard film is about 10 to 20 GPa. The results indicate that Co-DLC nanocomposites exhibit lower to large scale hardness than that of the a-C:H films.

The variation of hardness in the nanocomposites can be explained mainly in, terms of sp^3 C-C bonding present in the nanocomposite. It was observed that as the Co percentage in the nanocomposite increases the percentage of sp^3 C-C bonding decreases causing a decrease in the hardness. It has also been reported earlier that the presence of Co decreases the hardness of a-C:H nanocomposites[37].

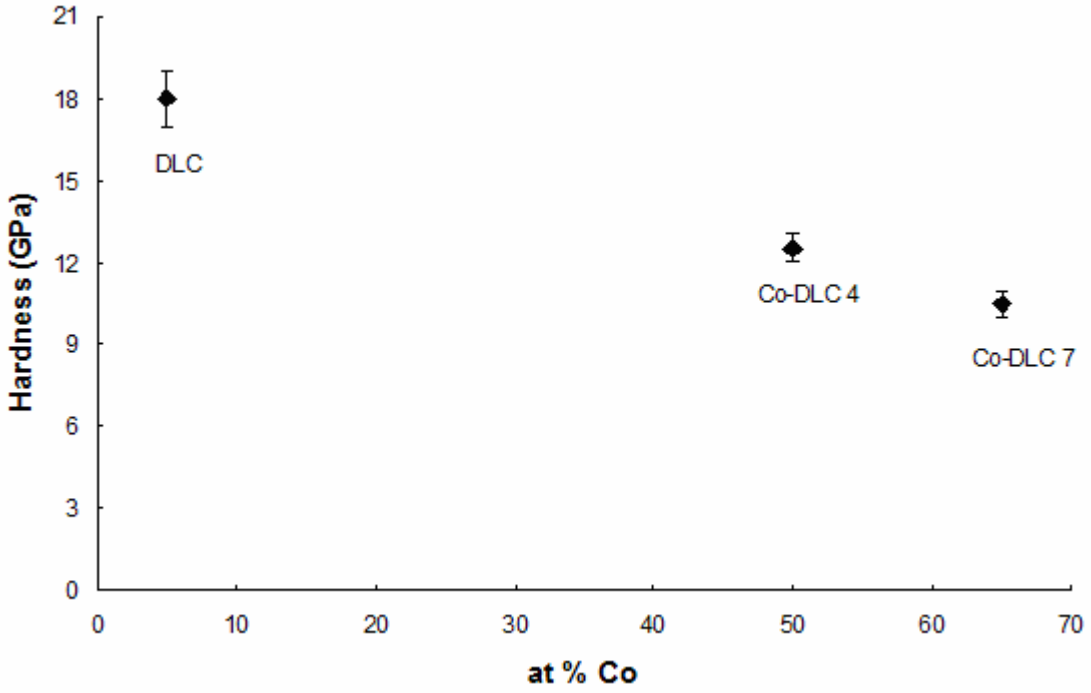

Figure 5.11 Variation of the microhardness with the percentage cobalt present in the Co-DLC nanocomposites.

It is well accepted that hardness is closely related to the sp^3 content and thus, the sp^3/sp^2 ratio in the nanocomposite. As pressure increases, the number of activated CH_4 molecules directed towards the substrate increases producing more DLC (hard) matrix. At lower pressure, a higher portion of CH_4 is sputtering the Co target suffering dissociation. Subsequent deposition of these species results in less sp^3 C-C bonding and lower hardness. This explains the trend of higher hardness of Nanocomposite 4 deposited at 35 mTorr pressure as compared to the hardness of Nanocomposite 7 deposited at 30 mTorr pressure. Nanocomposite 4 has higher sp^3 content and higher sp^3/sp^2 ratio and less percentage of Co as compared to Nanocomposite 7, this explains the decrease in the hardness for Nanocomposite 7. The results of the indentation test are in agreement with the results of XPS and FTIR results reported in the previous section.

5.7 Tribological Properties

Pin-on-disk experiments were performed to investigate the wear properties of the Co-DLC nanocomposites. DLC film is also shown here for comparison. Figure 5.12 demonstrates the variation of the coefficient of friction for DLC and Co-DLC Nanocomposites 4 and 7 as a function of sliding distance.

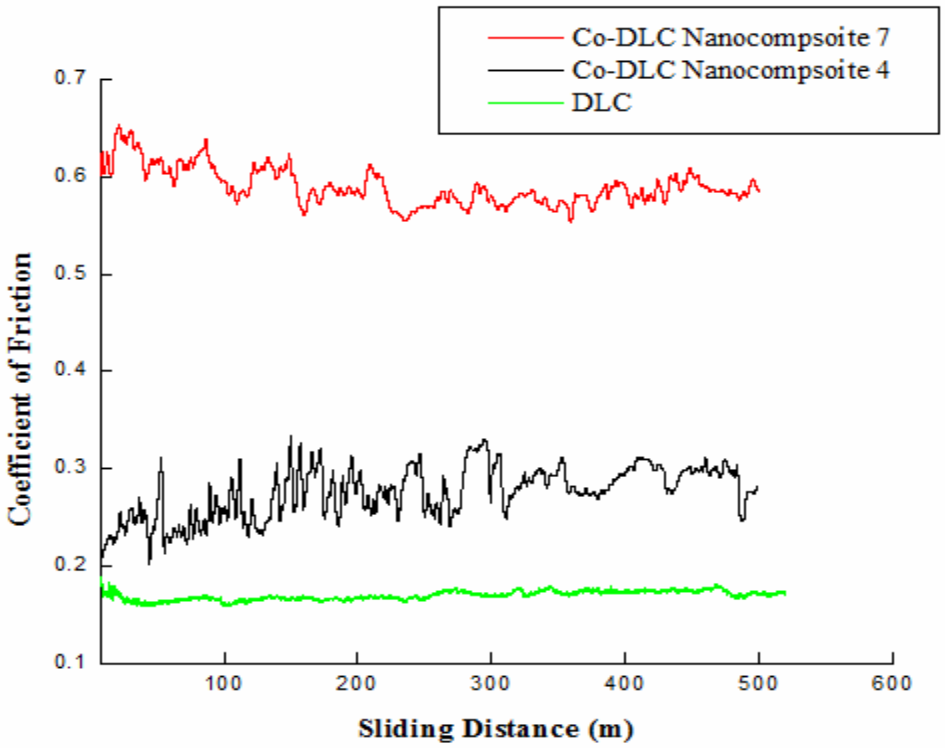

Figure 5.12 Variation of the coefficient of friction as a function of sliding distance for DLC and Co-DLC Nanocomposites 4 and 7.

The degree of sp^2 versus sp^3 bonding as well as relative amount of hydrogen and other alloying elements have strong influence on the coefficient of friction of the DLC films. The coefficient of friction for DLC is as low as 0.15. As the percentage of Co in the nanocomposites increases, the coefficient of friction also increases. The coefficient

of friction for Nanocomposite 4 (50 at % Co) was found to be 0.25 whereas that for Nanocomposite 7 (65 at % Co) is around 0.58. A higher C content (lower Co content), is translated into larger volume fraction of a-C:H that, exhibits low coefficient of friction. Low coefficient of friction requires the formation of a graphitic (sp^2) layer. So, higher metal content breaks up this lubricious transfer layer and increases the coefficient of friction. The coefficient of friction decreases with the increase in the sp^3/sp^2 ratio and percentage of hydrogen present in the nanocomposite. This trend that, has been observed in other Me-DLC films is confirmed for the selected nanocompsoites[37, 52].

5.8 Magnetic Properties

Figure 5.13 (a) shows the in plane magnetization-magnetic field hystersis loop for as deposited Co-DLC Nanocomposite 4, 5 and 7. For Nanocomposite 4 and 5, the magnetization does not reach saturation even for a magnetic field upto 15000 Oe. The coercivity and remanence are almost equal to zero, indicating the superparamgentic state of Co in the nanocomposite. As per previously reported studies, Co exists in the form of ε-Co which is a soft phase, and shows superparamagnetic behavior[59]. Whereas, Nanocomposite 7 shows coercivity of about 63.5 Oe suggesting that this film is still in the ferromagnetic state. The ferromagnetic nature of sample can be attributed to the presence of Co as HCP-Co. At higher percentage of Co the structure shows a combination of ε-Co and HCP-Co. As stated in the earlier section, Nanocomposite 7 shows large Co grains which agglomerate to form big Co particles and thus the HCP structure. Magnetization-magnetic field hystersis loop for Nanocomposite 4, 5 and 7

shows similar trend for out of plane applied field, as can be seen in Figure 5.13 (b). The curves are normalized as per the volume of the sample.

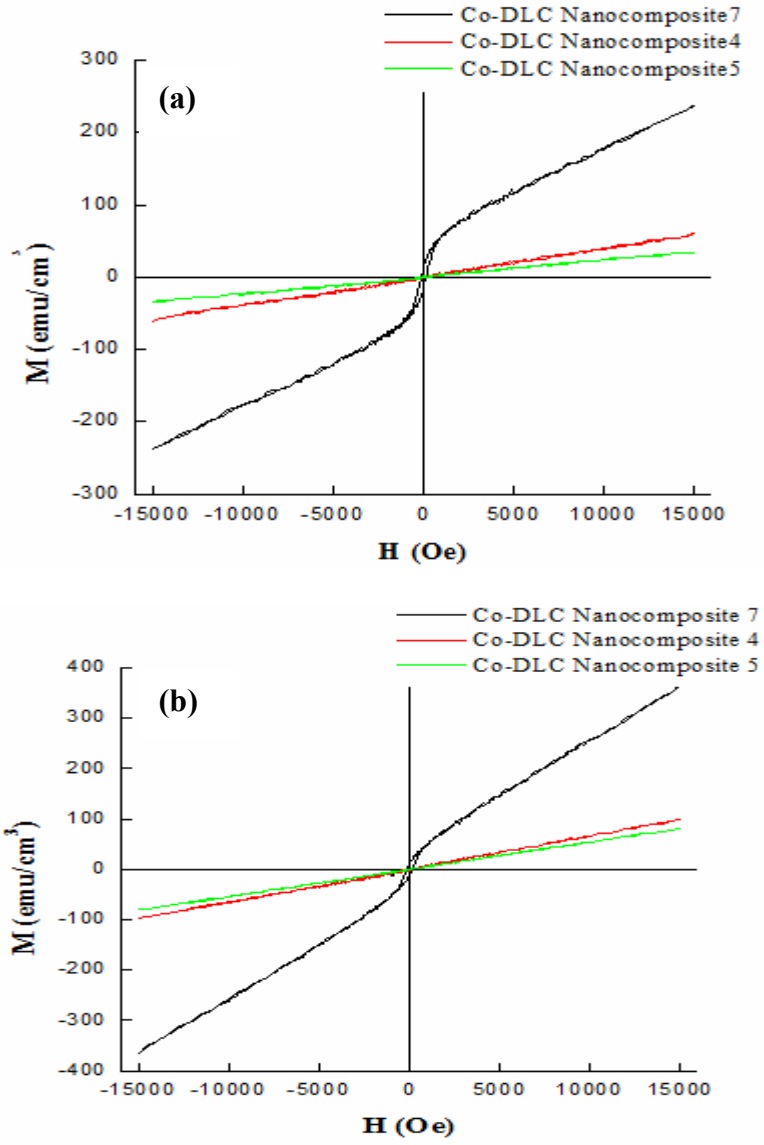

Figure 5.13 Magnetization-Magnetic field (M-H) hystersis curve for Co-DLC Nanocomposite 4, 5 and 7 for (a) in plane and (b) out of plane applied magnetic field.

The superparamagnetic behavior of Nanocomposite 4 and 5 can be attributed to the size of Co nanoparticles and exchange coupling in the magnetic domain. As stated earlier, each nanoparticle is a single domain magnet, with all the spins aligned in a single direction. As the nanoparticle size decreases, the number of spins exchange-coupled to resist spontaneous reorientation of magnetization also decreases. As reported in earlier section, Co-DLC Nanocomposites 4 and 7 show Co nanoparticles with size 12-18 nm and 5-9 nm, respectively, embedded in DLC matrix. These small particles are difficult to saturate and thus, show superparamgetic behavior. The results are also consistent with the large interparticle spacing for Nanocomposite 4 (2-3 nm) and 5 (4-5 nm). In Nanocomposite 7, Co particles agglomerate to form large size particles. Also small interparticle distance of about 1-2 nm, may lead to coupling interaction between two nanoparticles. Thus, Nanocomposite 7 shows small coercivity, indicating the ferromagnetic state of the sample.

As reported by previous studies, Co-DLC in as-deposited state shows highly defected ε-Co structure[1]. ε-Co, is a soft phase with magnetocrystalline anisotropy constant K equal to 1.5×10^6 erg/cm^3. Magnetocrystalline anisotropy is the energy necessary to deflect the magnetic moment in a single crystal from the easy to the hard direction. It strongly affects coercivity and remanence. Such a structure with small anisotropy constant results in superparamagentic state for small particle size of about 5-20 nm. As reported by Murray et al, ε-Co nanoparticle (9.5 nm in size), synthesized by chemical wet method also showed superparamagnetic behavior at room temperature[81].

Thus, Nanocomposites 4, 5 and 7 show the same trend of superparamagnetic and ferromagnetic behavior for both in plane and out of plane applied magnetic field.

5.9 Annealing Experiments

As reported earlier, as-deposited films of Co-DLC consist of metallic ε-Co embedded in amorphous carbon matrix. Annealing enhances the crystallinity of the defected Co phase by annihilating defects produced during sputter deposition. On annealing at 360^{o}C, Co-C thin film showed complete phase transformation from ε-Co to HCP Co and amorphous carbon transforms to graphite[1, 72-74]. So the samples were annealed to study the effect on sp^3 /sp^2 ratio with the change in the microstructure of the Co-DLC nanocomposite. Also, the effect of annealing and change in the microstructure on the magnetic properties of the nanocomposite was studied.

5.9.1 XPS

Figure 5.14 shows the high resolution spectra of C1s electron for (a) as-deposited Co-DLC Nanocomposite 4 and (b) Co-DLC Nanocomposite 4 annealed at 250^{o}C. The overall XPS spectrum for Nanocomposite 4 annealed at 250^{o}C exhibits C and Co peaks. Very small amount of oxygen was detected in the film indicating the absence of Co oxide formation in the annealed condition.

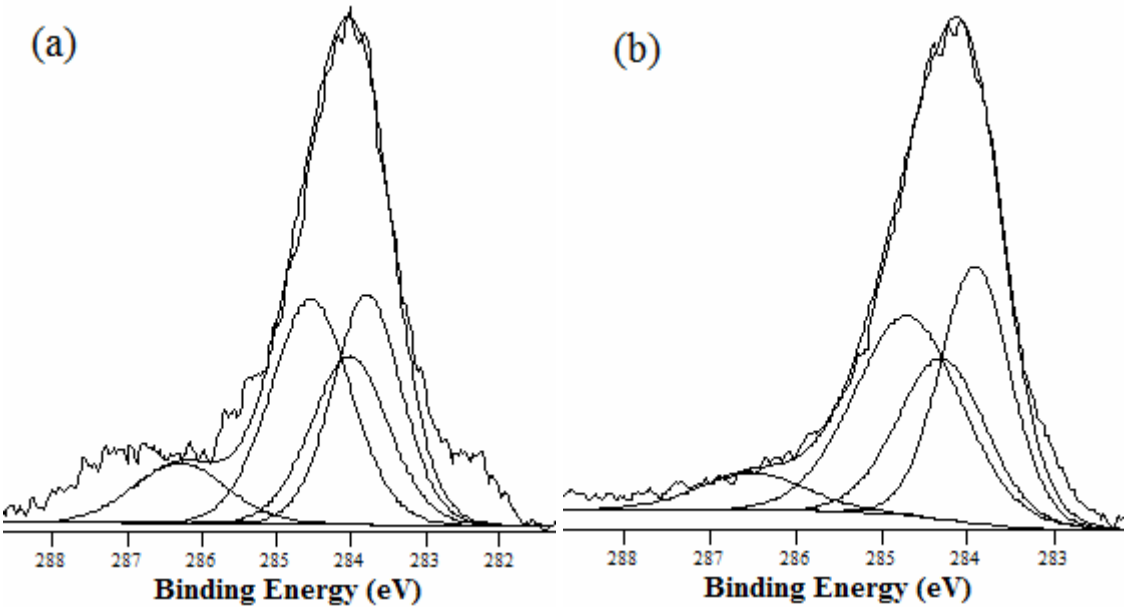

Figure 5.14 High resolution spectra of C 1s electron for Co-DLC Nanocomposite 4 (a) as deposited and (b) annealed at 250^{o}C.

The intensity and shape of the carbon peak in both as-deposited as well as annealed at 250^{o}C is almost equal. For further investigation, the high resolution spectrum of C 1s was deconvoluted into four different components as Co_xC at 283.5 eV, sp^2 C-C/C-H bond at 284.3 eV, sp^3 C-C/C-H bond at 284.8 eV and C-O bond at 286.5 eV. The nanocomposite shows presence of some C-O bonds. Some residual oxygen present in the chamber can possibly be incorporated into the film during deposition, interacting with carbon and hydrogen forming C-O or $–CH_2O-$ bonds. However, the percentage of C-O bond in overall composition of the nanocomposite is very small.

Table 5.5 The percentage of different states of carbon in C1s electron spectrum and overall composition of Nanocomposite 4.

	Binding Energy (eV)	**As-deposited Nanocomposite 4**		**Nanocomposite 4 annealed at 250°C**	
		% Conc. in C 1s Peak	**% Conc. in Nano-composite**	**% Conc. in C 1s Peak**	**% Conc. in Nano-composite**
Co_x-C	283.5	30.06	15.03	31.38	15.69
sp^2	284.3	24.74	12.37	24.73	12.36
sp^3	284.8	34.45	17.22	36.98	18.45
C-O	286.5	10.74	5.37	6.89	3.44

As per Table 5.5, the percentage of $sp^3$and sp^2 bonds in the case of both as deposited as well as nanocomposite annealed at 250°C is almost the same. This shows that upon annealing at 250°C, the chemical states of carbon remains the same; this is in agreement with the previously reported XPS studies on Co-DLC thin films[37].

5.9.2 Magnetic Properties

Co-DLC Nanocomposites 4, 5 and 7 were annealed at 250°C and 500°C for two hours in vacuum. The magnetic properties were measured for all the nine samples, i.e. as-deposited, 250°C annealed, 500°C annealed Co-DLC Nanocomposite 5 (25 at% Co), nanocomposite 4 (50 at% Co) and nanocomposite 7 (65 at% Co). The magnetic properties were measured for both conditions; in plane and out of plane applied magnetic field. In all cases, the hystersis curve shows the coercivity ranging from 65 Oe to 790 Oe. Thus, the nanocomposites show ferromagnetic behavior.

Figures 5.15 (a), (b) and (c), respectively illustrate the Magnetization-Magnetic field hystersis curve for annealed Co-DLC Nanocomposite 5, 4 and 7, for in plane applied magnetic field. The measured results, given in Table 5.6 show that the coercivity and saturation magnetization of nanocomposites increases with increase in the Co content as well as increase in the annealing temperature.

Nanocomposites 5, 4 and 7, show saturation magnetization of about 94 emu/cm^3, 192 emu/cm^3 and 588 emu/cm^3, respectively. The saturation magnetization of Co is 1400 emu/cm^3. So considering the Co content in the nanocomposites, the saturation magnetization for Nanocomposite 4, 5 and 7 should be higher than the given values. This decrease in the saturation magnetization may be due to the degradation of Co in the nanocomposite or may be attributed to the presence of non magnetic DLC phase.

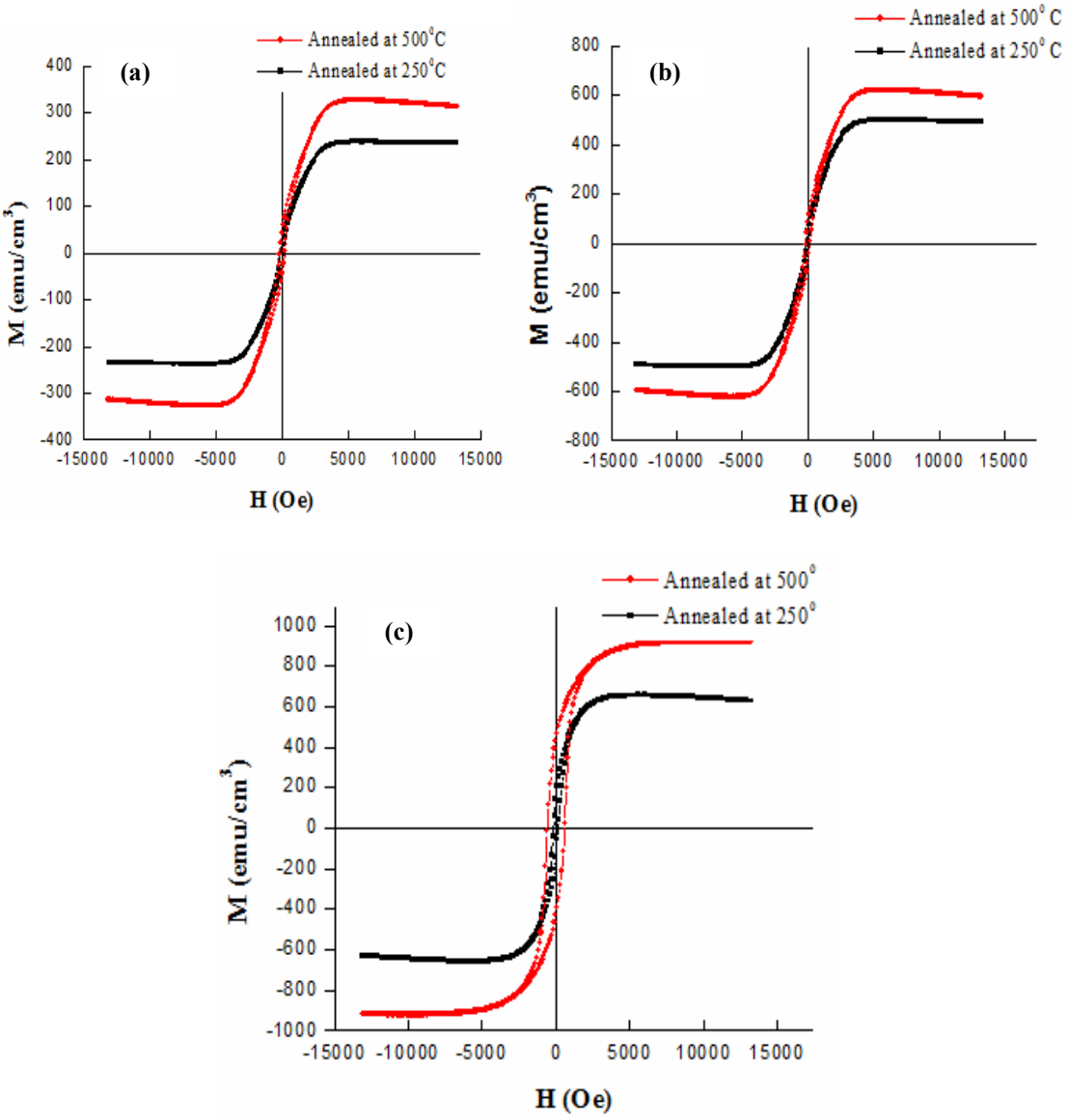

Figure 5.15 In plane Magnetization-Magnetic field hystersis curve for (a) Nanocomposite 5, (b) Nanocomposite 4 and (c) Nanocomposite 7, annealed at 250°C and 500°C.

Table 5.6 Magnetic properties for Co-DLC Nanocomposite 5, 4 and 7.

Nanocomposite	Condition	Applied Field	H_c (Oe)	M_s (emu/cm^3)	M_r (emu/cm^3)
5	Annealed at 250^{o}C	Parallel	65	234.57	23.13
	Annealed at 500^{o}C	Parallel	94	297.74	39.97
4	Annealed at 250^{o}C	Parallel	120	492.61	48.58
	Annealed at 500^{o}C	Parallel	192	595.48	79.80
7	Annealed at 250^{o}C	Parallel	160	628.47	142.09
	Annealed at 500^{o}C	Parallel	588	916.66	433.31

The enhancement in the coercivity and saturation magnetization of nanocomposites with annealing temperature can be attributed to the change in morphology of the nanocomposite and also change in the structure. As reported in the earlier studies, Co-C films annealed at 250^{o}C developed into FCC and HCP-Co. On further annealing at 500^{0}C, ε-Co completely transforms into HCP-Co[59, 81]. The anisotropy constant of HCP-Co is 4.4x10^{6}erg/cm^3, which is higher than anisotropy constant of ε-Co (4.4x10^{6}erg/cm^3), so coercivity increases.

The increase in the saturation magnetization of nanocomposites with increasing annealing temperature may also be attributed to the change in morphology. As reported by previous studies, the percentage of Co in nanocomposites increases with increase in the annealing temperature whereas, C content decreases[81]. So with increase in the Co content saturation magnetization too increases.

The higher coercivity and saturation magnetization of Nanocomposite 7, as compared to Nanocomposite 4 and 5, can be associated with the higher content of Co and size of Co nanoparticles. As reported in the previous section, in Nanocomposite 7, Co nanoparticles agglomerate and also the interparticle distance is very small. With increase

in the Co content by annealing, the Co particles may form a network and thus, increase exchange coupling between particles affecting the magnetic properties.

As discussed in an earlier section, TEM observations for both Nanocomposites 4 and 7 show a columnar structure. So the hystersis curve was acquired for the magnetic field perpendicular to the plane of the nanocomposites. Figures 5.16 (a), (b) and (c), respectively illustrate the Magnetization-Magnetic field hystersis curve for annealed Co-DLC Nanocomposite 5, 4 and 7, for out of plane applied magnetic field. The measured results, given in Table 5.7 show that the coercivity and saturation magnetization of nanocomposites increases with increase in the Co content as well as increase in the annealing temperature.

Table 5.7 Magnetic properties for Co-DLC Nanocomposite 5, 4 and 7.

Nanocomposite	**Condition**	**Applied Field**	**H_c (Oe)**	**M_s (emu/cm^3)**	**M_r (emu/cm^3)**
5	Annealed at 250^{o}C	Perpendicular	318	219.24	33.33
	Annealed at 500^{o}C	Perpendicular	404	305.09	47.04
4	Annealed at 250^{o}C	Perpendicular	606	440.45	63.34
	Annealed at 500^{o}C	Perpendicular	790	533.92	82.33
7	Annealed at 250^{o}C	Perpendicular	416	546.09	79.80
	Annealed at 500^{o}C	Perpendicular	709	816.17	190.038

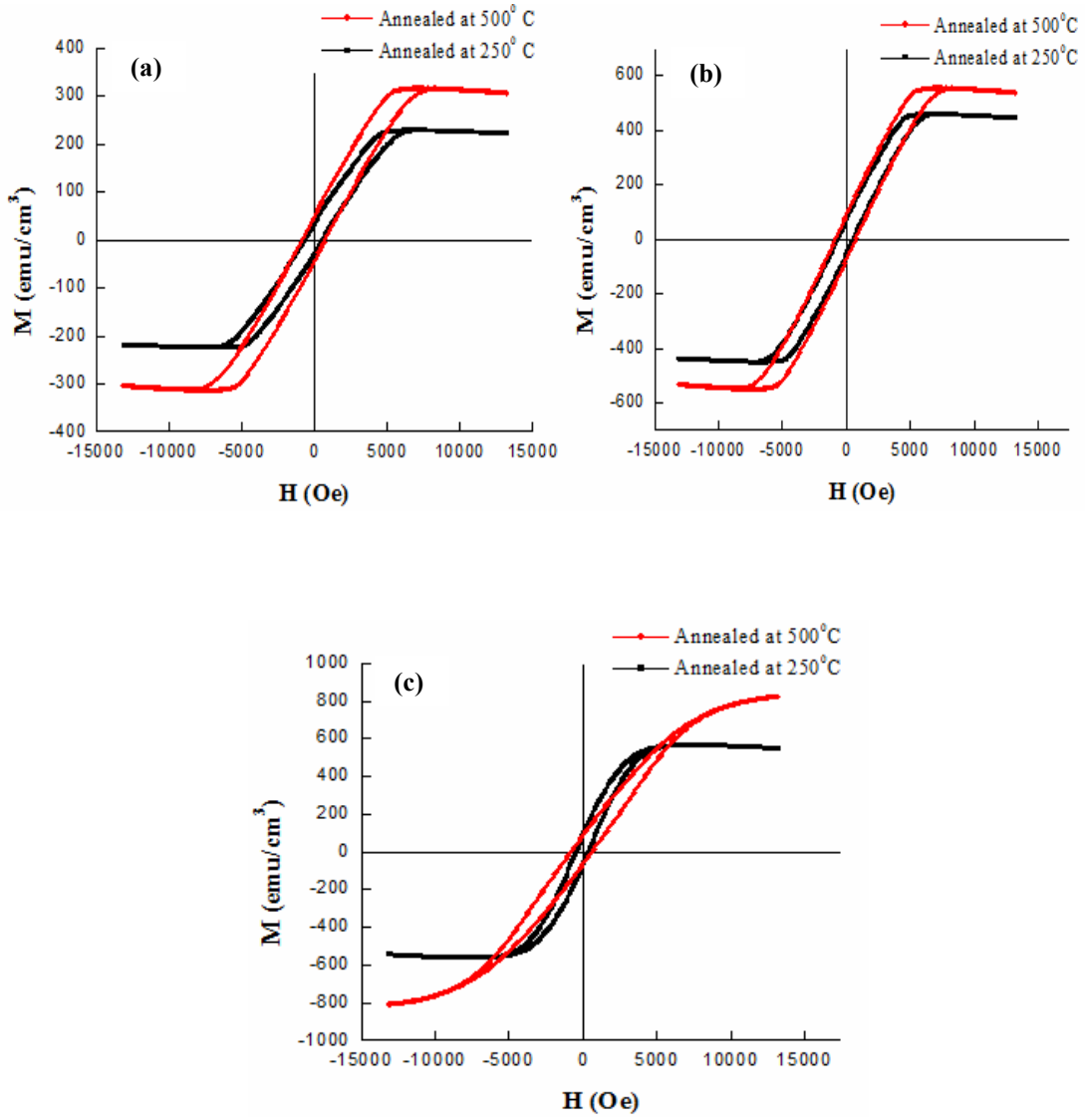

Figure 5.16 Out of plane Magnetization-Magnetic field hystersis curve for (a) Nanocomposite 5, (b) Nanocomposite 4 and (c) Nanocomposite 7 annealed at 250°C and 500°C.

Though the hystersis curve in this condition indicates that the sample is in the ferromagnetic state the shape of the curve is different from that in the parallel magnetic field. The hystersis curve shows the characteristic square shape for perpendicular field.

This is due to the texture of the sample. As discussed earlier, Nanocomposites 4 and 7 show a columnar structure embedded in the matrix. So, the square shape of the hystersis curve can be attributed to the interaction between the Co columns. Even though the columns are separated by DLC matrix, some interaction between the Cot columns is possible; giving the square shape hystersis curve.

The increase in the saturation magnetization and coercivity with increase in the annealing temperature in case of out of plane applied magnetic filed can again be attributed to the change of the ε-Co structure to HCP-Co and the morphology of the sample, as discussed for the in plane magnetic field.

In summary, the magnetic properties depend on the percentage, shape and size of the Co present that are also influenced by the annealing treatment. As-deposited Co-DLC films with 25 % and 50 % Co and small particles size of around 6-18 nm showed superparamgnetic behavior, whereas nanocomposite with 65 % Co showed ferromagnetic behavior. Saturation magnetization and coercivity increases with the increase in the Co content. Upon annealing, Co changes phase from ε-Co to HCP-Co, so saturation magnetization and coercivity increases. The hystersis curve for the film with the magnetic field applied in the direction perpendicular to the plane of the nanocomposite shows characteristics square shape. The square shape of the hystersis loop is because of the presence of columnar Co in the nanocomposites. Thus, optimum combination of Co concentration and annealing treatment can provide desirable magnetic properties. This principle can thus be used to tailor the properties of these nanocomposites, hence increasing their field of application.

5.10 Shelled Co/DLC Nanoparticles

After characterizing and comparing all the nanocomposites, Nanocomposite 4 was selected for the fabrication of Co/DLC shelled nanoparticles, due to its desirable mechanical, tribological and magnetic properties. Co-DLC thin film of about 20 nm, with Co Nanoparticles encapsulated in DLC matrix was deposited on the copper grid. The film was sandwiched between 5 nm of DLC layers. The copper grid was analyzed on TEM. Figure 5.17 shows Co nanocrystal of about 11-18 nm encapsulated by 2-3 nm thin DLC matrix. Most of the particles are single and are well separated by the DLC matrix. Based on the TEM observations and the mechanical, and tribological properties, the conditions for deposition of Co/DLC shelled nanoparticles were determined to further deposit a thin layer on Si substrate with the polystyrene 100 nm spheres deposited on a Si wafer.

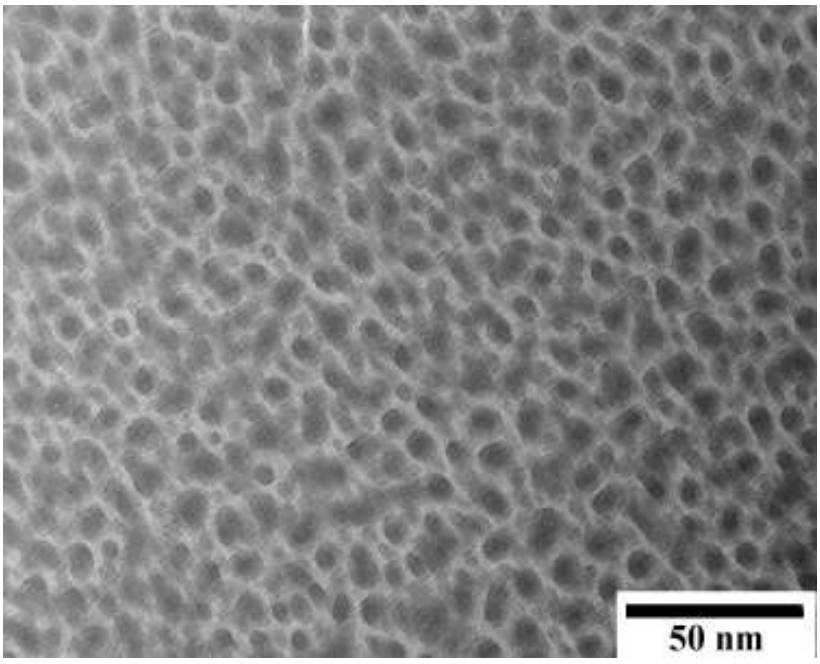

Figure 5.17 TEM image of Co-DLC thin film deposited on the copper grid.

The polystyrene spheres were deposited on the Si substrate by nanosphere lithography. Figure 5.18 shows a SEM micrograph of the Si substrate with the polystyrene spheres. The polystyrene spheres form a monolayer on the Si substrate and they are well dispersed on the Si substrate surface.

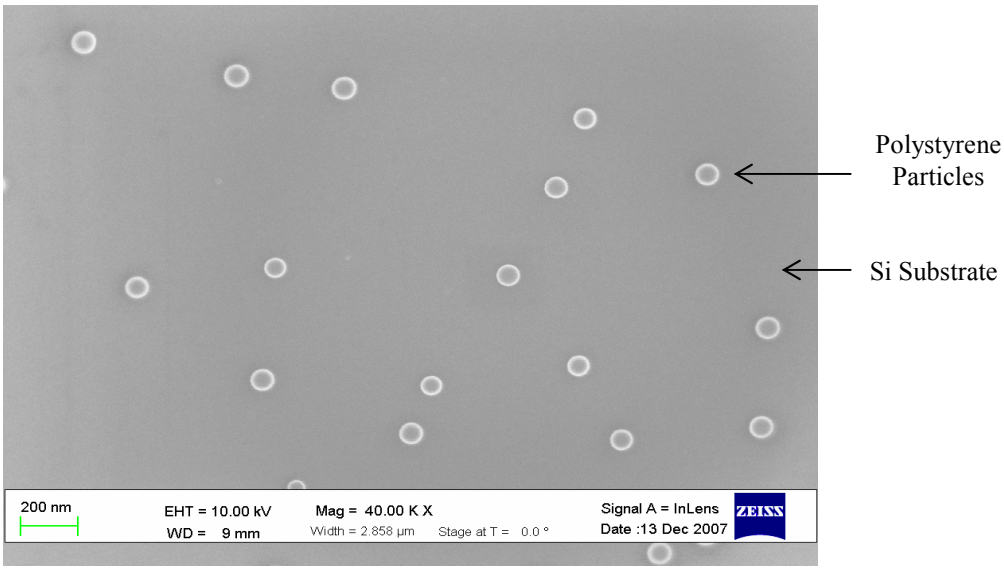

Figure 5.18 Si substrate with polystyrene particles.

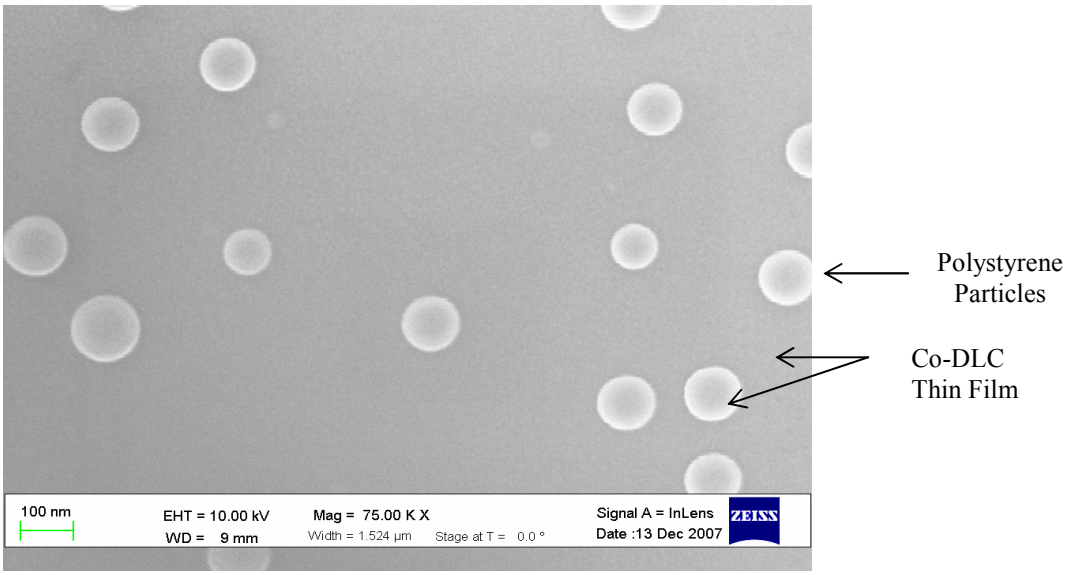

Figure 5.19 Si substrate and polystyrene particles with Co-DLC thin film.

The polystyrene spheres are used as the mask for the fabrication of shelled Co/DLC nanoparticles. A thin film of about 10 nm was deposited on the substrate in the PECVD/PVD system. Figure 5.19 shows the SEM micrograph of the Co-DLC coated polystyrene particles. The thin film covers the top surface of the polystyrene particles as well as the, Si substrate surface.

Following deposition, the Si wafer was immersed in the solvent Toluene to dissolve the polystyrene particles using an ultrasonic bath. The wafer was removed from the solvent and the solution was placed on a magnet. Figure 5.20 shows the SEM image of the substrate after the Toluene treatment. The SEM image shows that the polystyrene particles were dissolved by Toluene whereas Co-DLC thin film was present on Si substrate. The dark region in the micrograph represents the region of dissolved polystyrene particles.

Figure 5.20 Si substrate after dissolving polystyrene particles.

CHAPTER 6

CONCLUSIONS

Nanocomposite Co-DLC films were deposited using a hybrid CVD/PVD process. The nanocomposites were characterized using a variety of complimentary techniques and their structure and properties were investigated. Based on the results of the present study the following conclusions can be drawn:

- Co-DLC nanocomposites with Co content varying from 25 at% to 75 at% were synthesized successfully. The nanocomposites were consisting of ε-Co nanocolumns embedded in DLC matrix that was composed of sp^3 and sp^2 domains as shown by TEM, XPS and FTIR analyses. The nanocolumn size in the films exhibited a wide variation from 6 nm to 14 nm. Increasing Co content from 25 at% to 65 at% was found to increase Co nanocolumn size via reducing size variation and shifting the average size to higher values.
- Increasing Co content was found to decrease hardness from 18 GPa for pure DLC to about 9 GPa for films containing 65 at% Co. Also, tribological measurements showed an increase in the coefficient of friction from 0.1 for pure DLC to 0.25 for 50 at% Co and 0.6 for 65 at% Co.
- As-deposited Co-DLC films with 25 at% and 50 at% Co having small particles size showed superparamgnetic behavior, whereas nanocomposites with 65 at% Co and

larger average particle size showed ferromagnetic behavior. All three as-deposited films did not saturate.

- By annealing at 250^{o}C, all three nanocomposites exhibited ferromagnetic behavior, by increasing coercivity and saturation magnetization. Further annealing at 500^{o}C caused a phase transformation in Co from ε-Co to HCP-Co accompanied by a further increase in coercivity and saturation magnetization. The most dramatic increase was observed in the film with the highest Co content (65 at% Co) where the coercivity increased by a factor of 3.7 and the saturation magnetization by a factor of 1.5. The films with lower Co content exhibited also significant enhancement in coercivity and saturation magnetization. Thus, combination of Co concentration and an annealing treatment can be used to tailor the properties of Co-DLC nanocomposites, thus, increasing their field of application.

REFERENCES

1. X. Nie, J. C. Jiang, E. I. Meletis, L. D. Tung, L. Spinu, Journal of Applied Physics, 93 (2003) 4750.
2. G.F. Huang, Z. Lingping, H. Weiqing, Z. Lihua, L. Shaolu, L. Dey, Diamond and Related Materials, 12 (2003) 1406.
3. A. Erdemir, I.B. Nilufer, O.L. Eryilmaz, M. Beschliesser, G.R. Fenske, Surface and Coatings Technology, 120–121 (1999) 589.
4. S.K. Field, M. Jarratt, D.G. Teer, Tribology International, 37 (2004) 949.
5. A Grill, Diamond and Related Materials, 12 (2003) 166.
6. V. Tiainen, Diamond and Related Materials, 10 (2001) 153.
7. J. Ting, H. Lee, Diamond and Related Materials, 11 (2002) 1119.
8. J. Choi, M. Kawaguchi, T. Kato, M. Ikeyama, Microsyst Technol, 13 (2007) 1353.
9. R.J. Narayan, H. Abernathy, L. Riester, C.J. Berry, R. Brigmon, Journal of Materials Engineering and Performance, 14 (2005) 435.
10. N. Yao, A.G. Evans, C.V. Cooper, Surface and Coatings Technology, 179 (2004) 306.
11. V. Singh, J.C. Jiang, E.I. Meletis, Thin Solid Films, 489 (2005) 150.
12. A. V. Kolobov, J. Tominaga, T. K. Zvonareva, V. I. Ivanov Omskii, Journal of Applied Physics, 92 (2002) 6195.
13. C. Laurent, E. Kay, Journal of Applied Physics, 65 (1989) 1717.

14. C. Laurent, D. Mauri, E. Kay, S. S. P. Parkin, Journal of Applied Physics, 65 (1989) 2017.
15. F. L. Wang, J. C. Jiang, E. I. Meletis, Applied Physics Letters, 83 (2003) 2423
16. F. L. Wang, J. C. Jiang, E. I. Meletis, Journal of Applied Physics, 95 (2004) 5069.
17. E. I. Meletis, J. C. Jiang, Journal of Nanoscience and Nanotechnology, 6 (2006) 1.
18. R. Skomski, Journal of Physics: Condensed Matter, 15(2003) R 841.
19. B. Cullity, Introduction to Magnetic Materials, Addison Wisley Publication, (1972).
20. N. A. Spaldin, Magnetic Materials: Fundamentals and Device Applications, Cambridge University Press, (2003).
21. W.D. Callister, Fundamentals of Materials Science and Engineering, John Wiley and Sons Publication, (2003).
22. C. Kittel, Introduction to Solid State Physics, John Wiley and Sons Publication, (1996).
23. R.H. Kodama, Journal of Magnetism and Magnetic Materials, 200 (1999) 359.
24. C. Casiraghia, A.C. Ferrari, R. Ohr, D. Chu, J. Robertson, Diamond and Related Materials, 13 (2004) 1416.
25. D.R. McKenzie, S.C.H. Kwok, M.M. Bilek, D.G. McCulloch, P.K. Chu, Physica B, 394 (2007) 273.
26. I. Bergenti, A. Riminucci, E. Arisi, M. Murgia, M. Cavallini, M. Solzi, F. Casoli, V. Dediu, Journal of Magnetism and Magnetic Materials, 316 (2007) 987.
27. N. Gopinathan, C Robinson, F. Ryan, Thin Solid Films, 355-356 (1999) 401.
28. C. Berryl, A. Curtis, Journal of Physics D: Applied Physics, 36 (2003) R189.

29. P. Sharma, S. Brown, G. Walter, S. Santra, B. Moudgil, Advances in Colloid and Interface Science, 123–126 (2006) 471.

30. M. D. Shultza, S. Calvin, P. P. Fatouros, S. A. Morrisona, E. Carpenter, Journal of Magnetism and Magnetic Materials, 311 (2007) 464.

31. A. Jordan, R. Scholz, P. Wust, H. Fahling, R. Felix, Journal of Magnetism and Magnetic Materials, 201 (1999) 413.

32. A. Ito, M. Shinkai, H. Honda, T. Kobayashi, Journal of Bioscience and Bioengineering, 100 (2005) 1.

33. S. Rana, A. Gallo, R.S. Srivastava, R.D.K. Misra, Acta Biomaterialia, 3 (2007) 233.

34. M. J. Wozniak, P. Wozniak, M. Bystrzejewski, S. Cudzilo, A. Huczko, P. Jelen, W. Kaszuwara, J. A. Kozubowski, H. Lange, M.n Leonowicz, M. Lewandowska-Szumiel, Journal of Alloys and Compounds, 423 (2006) 87.

35. T. Neuberger, B. Schopf, H. Hofmann, M. Hofmann, B. Rechenber, Journal of Magnetism and Magnetic Materials, 293 (2005) 483.

36. J. Robertson, Materials Science and Engineering, R37 (2002) 129.

37. F. Wang, Multifunctional Nanocomposite Co-containing Diamondlike Carbon Thin Films, Ph.D. Dissertation, Louisiana State University, (2004).

38. H. X. Li, T. Xu, J. M. Chen, H. D. Zhou, H.W. Liu, Applied Surface Science, 227 (2004) 364.

39. P.Gupta, V. Singh, E.I. Meletis, Tribology International, 37 (2004) 1019.

40. J. Robertson, Diamond and Related Materials, 6 (1997) 212.

41. G. Dearnaley, J. H. Arps, Surface and Coating Technology, 200 (2005) 2518.

42. A. Grigonis, Z. Rutkuniene, V. Kopustinskas, G.J. Babonas, A. Reza, Vacuum, 78 (2005) 593.
43. K. Yamamoto, K. Wazumi, T. Watanabe, Y. Koga, S. Iijima, Diamond and Related Materials, 11 (2002) 1130.
44. M.C. Polo, J.L. Andujar, A. Hart, J. Robertson, W.I. Milne, Diamond and Related Materials, 9 (2000) 663.
45. S. Swann, Physics Technology, 19 (1998) 67.
46. J. M. Lackner, C. Stotter, W. Waldhauser, R. Ebner, W. Lenz, M. Beutl, Surface and Coatings Technology, 174 –175 (2003) 402.
47. C. Corbella, M. Vives, G. Oncins, C. Canal, J.L. Andujar, E. Bertran, Diamond and Related Materials, 13 (2004) 1494.
48. C. Casiraghi, A. C. Ferrari, J. Robertson, Physical Review B, 72 (2005) 085401.
49. J. Robertson, Thin Solid Films, 383 (2001) 81.
50. A. Erdemir, C. Donnet, Journal of Applied Physics, 39 (2006) R311.
51. R. Haerle, E. Riedo, A. Pasquarello, A. Baldereschi, Physical Review B, 65 (2001) 045101.
52. V. Singh, Synthesis, Structure, and Tribological Behavior of Nanocomposite DLC Based Thin Films, Ph.D. Dissertation, Louisiana State University, (2004).
53. C. Wang, S. Yang, H. Li, J. Zhang, Journal of Applied Physics, 101 (2007) 013501.
54. J. Robertson, Physical Review Letters, 68 (1992) 220.
55. J. Sui, W. Cai, Surface and Coatings Technology, 201 (2006) 1323.
56. J. Goldsmitha, E. Sutter, J.J. Moore, B. Mishra, M. Crowder, Surface and Coatings Technology 200 (2005) 2386.
57. S. H. Liou, M. Zheng, M. L. Yan, R. Skomski, N. I. Polushkin, D. J. Sellmyer, Scripta Material, 44 (2004) 1347.

58. B. Jiang, D. Yang, A. N. Ulyanov, S. Yu, Journal of Applied Physics, 95 (2004) 7115.

59. J. Delaunay, T. Hayashi, M. Tomita, S. Hirono, Journal of Applied. Physics, 36 (1997) 7801.

60. K. Bewilogua, R. Wittorf, H. Thomsen, M. Weber, Thin Solid Films, 447-448 (2004) 142.

61. J. Huo, H. Song, X. Chen, S. Zhao, C. Xu, Materials Chemistry and Physics, 101 (2007) 221.

62. X. He,W. Li, H. Li, Surface and Coatings Technology, 84 (1996) 414.

63. H. Wang, S. P. Wong, W. F. Lau, X. Yan, X. Lu, W. Y. Cheung, N. Ke, Thin Solid Films, 382 (2001) 133.

64. D. Liu, G. Benstetter, W. Wang, J. Zhang, Journal of Vaccum Science Technology, 22 (2006) 2329.

65. J. Henry, J. Scott, and S. A. Majetich, Physical Review B, 52 (1995) 12 564.

66. Y. Liu, J. Ling, X. Zhang, Nanotechnology, 15 (2004) 43.

67. M. P. Delplancke-Ogletree, O.R. Monteiro, Surface and Coatings Technology, 108-109 (1998) 484.

68. S. Chowdhury, M.T. Laugier, I.Z. Rahman, Thin Solid Films, 468 (2004) 149.

69. S. Chowdhury, M. T. Laugier, I. Z. Rahman, Journal of Materials Processing Technology, 153-154 (2004) 804.

70. J.X. Guo, B.K. Tay, X.W. Sun, X.Z. Ding, D.H.C. Chua, Surface and Coatings Technology, 169 –170 (2003) 393.

71. X. Nie, J. C. Jiang, L. D. Tung, L. Spinu, E. I. Meletis, Thin Solid Films, 415 (2002) 211.

72. H. Wang, M. F. Chiah, W. Y. Cheung, S. P. Wong, Physica B, 344 (2004) 88.

73. S. Tajima, S. I. Hirano, Journal of Materials Science Letters, 11 (1992) 22.

74. H. Y. Sun, S. Z. Feng, X. F. Nie, Y. P Sun, Journal of Magnetism and Magnetic Materials, 299 (2006) 70.

75. C. J. Sun, G. M. Chow, Y. Zhao, Y. K. Hwu, J. P. Wang, Journal of Magnetism and Magnetic Materials, 303 (2006) e383.

76. D. L. Pelecky, X. Q. Zhang, R. D. Rieke, Journal of Applied Physics, 79 (1996) 5312.

77. D. Chua, W. I. Milne, B. K. Tay, P. Zhang, X. Z. Ding, Journal of Vacuum Science Technology, A21 (2003) 353.

78. V. Palshin, E. I. Meletis, S. Ves, S. Logothetidis, Thin Solid Films, 270 (1995) 165.

79. Y. Liu, E. I. Meletis, Journal of Materials science , 32 (1997) 3491

80. Y. Liu, A. Erdemir, E. I. Meletis, Surface Coating Technology, 82 (1996) 48.

81. C. B. Murray, S. Sun, H. Doyle, T. Betley, Mater. Res. Bull. 26, (2001) 985.

BIOGRAPHICAL INFORMATION

Gunjan Shebe was born in Nagpur, Maharashtra, India. She received her Bachelors of Engineering degree in Metallurgy from Visvesvaraya National Institute of Technology Nagpur, India. She worked with Cummins India Limited Pune, R&D and Engineering Division. In Fall 2006 she started her graduate studies in Materials Science and Engineering at University of Texas at Arlington, completing it by Fall 2007. Her research interest includes fabrication and characterization of Nanocomposites.